Structures 84 (2026) 110936

Contents lists available at ScienceDirect

Structures

journal homepage: www.elsevier.com/locate/structures

Influence of metal transfer modes and process conditions on WAAM-fabricated AM46 carbon steel walls

T. Tankova [a], C. Zhu [b,c], H. El Bamby [a], K. Monteiro [b], S. Sabari [b], L. Simões da Silva [b,*], D.G. Andrade [b]

[a] Department of Engineering Structures, Delft University of Technology, Delft, the Netherlands
[b] University of Coimbra, ISISE, ARISE, Department of Civil Engineering, Coimbra, Portugal
[c] University of Coimbra, CEMMPRE, ARISE, Department of Mechanical Engineering, Portugal

ARTICLE INFO

Keywords:
Wire Arc Additive Manufacturing
Steel
Process window
Welding parameters
Microstructure
High strength steel

ABSTRACT

Wire Arc Additive Manufacturing (WAAM) holds significant potential for the fabrication of intricate, medium to large-scale metallic components. However, current research predominantly targets lab-scale specimens, often exploring limited ranges of process parameters and overlooking the complex interactions between thermal, geometrical, and mechanical factors. In this study, a comprehensive experimental program is conducted to systematically investigate the influence of key process parameters, namely current, voltage, wire feed speed, and travel speed, across three Gas Metal Arc Welding (GMAW) transfer modes: Cold Metal Transfer (CMT), Conventional Spray (S-GMAW), and Pulsed Current (P-GMAW). 3Dprint AM 46 carbon steel was used as the feedstock material. The investigation proceeded in three stages: development of a broad process window (produced by CMT), characterisation of 10-layer walls (produced by CMT, S-GMAW and P-GMAW), and mechanical testing of large-scale walls (produced by P-GMAW) to construct a process–property map. Experimental characterisation revealed that the heat input (HI) and the wire feed speed to travel speed (WFS/TS) ratio govern the cooling time ($\Delta t_{8/5}$), which exhibited a linear dependence on HI. Bead width and height were governed by combined effects of HI and WFS/TS, while hardness, yield strength, and ultimate tensile strength followed inverse power-law correlations with HI. Ultimate strain showed a positive correlation with HI. In parallel, an analytical modelling framework is proposed to establish predictive equations linking process parameters with thermal cycles, deposition geometry, and mechanical properties. These models aim to accelerate process planning and enable property-driven slicing strategies for WAAM structural applications.

1. Introduction

Wire Arc Additive Manufacturing (WAAM) offers significant advantages for structural-scale fabrication, including near-net-shape production, reduced material waste, lower embodied carbon and energy footprints, and complete digital control over process parameters [1–3]. While its application has been demonstrated in laboratory settings, the commercialisation of WAAM for large-scale structural components remains limited due to challenges in process reliability, quality assurance, and parameter selection. These limitations underline the urgent need for process standardisation and predictive modelling to facilitate consistent, high-quality production. To advance WAAM toward industrial adoption, it is essential to establish a robust process parameter window and develop analytical models that link key input parameters with resulting part geometry, thermal cycles, and mechanical performance.

Metal transfer modes play a crucial role in WAAM by governing the arc stability heat input, and fluid flow dynamics, all of which critically influence the final geometry, microstructure, and mechanical properties of the built components [4]. Over time, significant advances have been made in refining these modes, such as Cold Metal Transfer (CMT), Pulsed and Spray transfer modes, each offering distinct thermal profiles and deposition characteristics. For instance, Mukherjee et al. [5] demonstrated that metal transfer modes alter the solidification patterns, grain structure and grain orientations. Zhu et al. [6] identified that the pulsed transfer mode offers superior thermal and mechanical characteristics required for the WAAM compared to other modes. Luo et al. [7] compared and found that the manufacturing efficiency of pulsed arc is higher than that of the non-pulsed arc at similar arc power due to the high deposition rate. Recent advancements coupled electronic control

* Corresponding author.
E-mail address: luisss@dec.uc.pt (L.S. da Silva).

https://doi.org/10.1016/j.istruc.2025.110936
Received 17 August 2025; Received in revised form 1 November 2025; Accepted 14 December 2025
Available online 16 December 2025

Nomenclature

B_{f_u}	Exponent for ultimate tensile strength model
B_{f_y}	Exponent for yield strength model
B_{ε_u}	Exponent for ultimate strain
B_h	Exponent for layer height evolution
B_E	Exponent for Young's modulus model
B_{HV}	Exponent for hardness model
B_w	Exponent for bead width evolution
a_{f_u}	Pre-exponential factor for ultimate tensile strength model
a_{f_y}	Pre-exponential factor for yield strength model
a_{ε_u}	Pre-exponential factor for ultimate strain
a_h	Pre-exponential factor for layer height evolution
a_{HV}	Pre-exponential factor for hardness model
a_w	Pre-exponential factor for bead width evolution
a_i	Empirical constant for heat input model
C	Current
CMT	Cold Metal Transfer
CTWD	Contact-Tip-to-Work Distance
E	Young's modulus
f_u	Ultimate Tensile Strength
f_y	Yield Strength
GMAW	Gas Metal Arc Welding
GTAW	Gas Tungsten Arc Welding
h	layer height
HAZ	Heat-Affected Zone
HI	Heat Input
K_1	Coefficient of the bilinear plus nonlinear hardening model
K_2	Coefficient of the bilinear plus nonlinear hardening model
K_3	Coefficient of the bilinear plus nonlinear hardening model
K_4	Coefficient of the bilinear plus nonlinear hardening model
PAW	Plasma Arc Welding
P-GMAW	Pulse Gas Metal Arc Welding
R^2	Coefficient of determination
S-GMAW	Spray Gas Metal Arc Welding
TS	Travel Speed
V	Voltage
w	bead width
WAAM	Wire Arc Additive Manufacturing
WFS	Wire Feed Speed
$\Delta t_{8/5}$	Cooling time between 800 and 500 °C
ε_f	Elongation at fracture
ε_{sh}	Strain at the end of the yielding plateau and start of strain hardening
ε_u	Ultimate strain
ε_y	Strain at yield point (onset of yielding plateau)
a_E	Pre-exponent for Young's modulus model

alongside mechanical control, such as CMT welding, which combines short circuiting transfer with mechanical wire oscillation to achieve low heat input and spatter in WAAM products [8–11]. These studies emphasised how tailored transfer modes directly influence solidification kinetics, microstructure formation, and production efficiency.

Beyond metal transfer modes, deposition quality is influenced by a web of interdependent parameters, including electrical variables such as current and voltage, mechanical parameters such as wire feed speed, deposition speed, contact-tip-to-work distance (CTWD) and torch angle, substrate conditions such as preheat temperature, material type, thickness and interpass temperature, and environmental factors such as shielding gas composition and flow rate [9]. Among these factors, the current and travel speed are the key parameters having a significant effect on the deposited material from microstructure to geometry [11]. The CTWD alters the arc length and regulates the voltage to stabilise the arc stability, which in turn governs the heat input [12]. There are studies reporting on the importance of the shielding gas as well on the weld bead height, or porosity sensitivity, depending on the gas flow rate [13–15]. The selection of substrate material parameters such as pre-heating temperature, surface condition, alloy type and thickness have a strong effect on the WAAM product quality [16–18]. However, most of these studies focusing on isolated parameters generally overlook the synergistic interaction between the parameters, which is a critical limitation for the holistic framework for the WAAM process optimisation.

A few studies have proposed alternative approaches to the WAAM process by introducing secondary parameters derived from combinations of primary welding variables, including current, voltage, wire feed speed and travel speed. These secondary parameters are intended to capture the interaction effects between multiple variables in a more compact and interpretable form. For instance, Adebayo et al. [19] used *WFS/TS* ratio as the controlling parameters to optimise the bead height and width, which is a ratio between the feed speed (*WFS*) and travel speed (*TS*). Similarly, Rosli et al. [20] report the usage of heat input as the controlling parameter that includes the effects of current, voltage, travel speed and efficiency, which is a function of these welding parameters and travel speed, to achieve the higher tensile strength and microhardness.

Table 1 provides a comparative overview of recent studies focusing on the WAAM of low-carbon steels, which are widely used in structural and industrial applications [21–37] These works predominantly emphasise the role of heat input as a primary factor influencing bead geometry, microstructure formation, hardness, and tensile performance. Although the influence of heat input is consistently reported, most of these investigations explored only narrow parameter ranges and typically relied on trial-and-error approaches to produce isolated defect-free walls. This limited scope has resulted in a lack of systematic exploration across a broad spectrum of process parameters and metal transfer modes. Moreover, the interaction between multiple parameters, such as current, travel speed, and transfer mode, has not been sufficiently studied in an integrated framework.

Crucially, these studies often focus solely on one transfer mode, and few address the full spectrum of relationships among process parameters, thermal cycles, geometric evolution, such as layer height and bead width, and mechanical properties. As a result, developing predictive models or adaptable parameter frameworks for complex geometries and large-scale structures remains an unresolved challenge. This gap is particularly limiting for practical applications, where varying geometry, orientation, and wall thickness demand tailored parameter selection across different regions of the same part [38]. To enable industrial-scale deployment and automation of WAAM, there is an urgent need for a robust, experimentally validated process framework that links process parameters to the final structural integrity of the components.

Addressing the demands of civil engineering applications and the identified research gaps, this study adopts a structured three-stage methodology to investigate the process–structure–property relationships in WAAM carbon steel fabricated walls. First, an extensive process parameter window was developed using the CMT mode to identify stable and unstable deposition conditions. In the second stage, 10-layer walls were produced using CMT, Pulsed Gas Metal Arc Welding (P-GMAW), and Spray Gas Metal Arc Welding (S-GMAW) to examine the influence of process parameters on thermal history, bead geometry, microstructure and hardness. Finally, full-scale P-GMAW walls were mechanically tested to develop a mechanical property–process map. In

Table 1
Summary of the recent research works on WAAM of low-carbon steel.

Author name & year	Material	WAAM process	Metal transfer mode	Parameters range			Observations
				Current [A]	Voltage [V]	Travel speed [mm/s]	
Rafieazad et al., 2019 [32]	ER70S-6	GMAW	Short-circuit	320	28.0	5	Fine polygonal ferrite with pearlite formed the dominant microstructure; bainite and acicular ferrite appeared at melt-pool boundaries. Yield and tensile strengths were similar in horizontal and vertical directions.
Dirisu et al., 2019 [30]	ER70S-6, ER90S-B3, ER120S-G	GMAW	CMT	157	13.3	6.7	The study demonstrates that the hardening and softening regions in the layer bands owing to heat input and resultant microstructures can be overcome by adopting optimum repair strategies.
Le et al., 2020 [33]	ER70S-6	GMAW	-	50, 100	18.0	5	Deposition strategy and heat input were found to significantly affect geometric regularity and hardness distribution, while tensile properties showed moderate anisotropy.
Aldalur et al., 2020 [29]	ER70S-6	GMAW	Synergic pulse	229, 244	27.1, 26.6	3.3, 10.8	The study explores varying repair strategies and finds that oscillatory deposition techniques significantly enhance productivity.
Ayan and Kahraman 2021 [34]	ER70S-6	GMAW	-	90, 100	23.0	16.7	WAAM was performed using two torch movements. Mechanical properties were consistent across orientations. Minor microstructural and layer morphology differences were observed.
Astarita et al., 2021 [35]	ER70S-6	GMAW	-	80	18.0	3.3	Mechanical properties assessed via Digital Image Correlation showed negligible anisotropy between deposition and stacking directions. Tomography detected voids, although they had no significant effect on tensile strength.
Xin et al., 2021 [28]	ER70S-6	GMAW	-	-	-	-	A calibrated material model is developed through experimental and numerical analyses to accurately represent the behaviour of WAAM components across different printing orientations.
Tankova et al., 2022 [36]	ER70S-6	GMAW	CMT	155	15.7	10	Machined samples showed higher strength and ductility than as-built. Optical and SEM analyses revealed ductile failure and annealed ferritic microstructure. Tensile results confirmed mechanical isotropy and compliance with Eurocode 3 structural steel standards.
Huang et al., 2022 [26]	ER70S-6, ER110S-G	GMAW	Pulsed Short-circuit	130 54	24.8 14.8	6.7 5	A comparison between the two metal transfer modes indicates that pulsed transfer is more suitable for bulk deposition, providing precise heat control and higher peak temperatures, whereas short-circuit transfer better controls bead geometry at lower heat inputs, making it advantageous for thin and complex shapes.
Bellamkonda et al., 2022 [27]	ER70S-6	GMAW	Pulse CMT Pulse	272 170	16.2 13.8	5.8 5.8	Pulsed CMT is shown to achieve superior mechanical properties compared to pulsed GMAW, attributed to the formation of finer grains resulting from lower heat input.
Nagasaki et al. 2022 [37]	ER70S-6	GMAW	Pulse CMT Pulse	229 200	18.3 16.0	6.7 6.7	Cylindrical WAAM components were fabricated using GMAW and CMT. Mechanical performance correlated with microstructural refinement driven by heat input differences.
Mohammadi et al., 2024 [21]	ER70S-6	GMAW	Pulsed	80	19.0	7	The study investigates the influence of four pulse frequency levels to achieve isotropic and enhanced mechanical properties in WAAM walls.
Panicker et al., 2024 [22]	ER70S-6	GMAW	Rotational Arc	200	-	-	A rotational arc technique is employed to uniformly distribute heat, thereby minimising localised overheating and inconsistent HAZ formation, which leads to improved mechanical properties.
Dekis st al, 2024 [23]	ER70S-6	GTAW	Pulse	300	-	2, 2.5, 3	Three travel speed ranges are evaluated, revealing that TS significantly affects the balance between heat input and cooling rate, thereby enhancing mechanical properties.
Zhai et al., 2024 [24]	ER70S-6	PAW	-	203	27	3.8	The study successfully demonstrates the feasibility of Plasma Arc Welding (PAW) for additive manufacturing and confirms that post-heat treatment improves the mechanical performance of WAAM specimens.
Badoniya et al., 2024 [25]	ER70S-6	GMAW	-	-	18	4, 7, 10	Travel speed is identified as a critical parameter influencing bead width, height, and penetration, primarily due to its effect on the resulting heat input.
Chen et al. 2025 [31]	ER70S ER120S	GMAW	-	160	14.8	13.3	Investigated mechanical and microstructural properties of WAAM-fabricated normal- and high-strength steels. Reported near-isotropic tensile behaviour, consistent yield and ultimate strengths, and homogeneous ferrite–pearlite microstructure across build orientations.

The boxes marked with a '–' symbol indicate that the respective information was not reported by the authors.

total, approximately 70 samples were fabricated and analysed under systematically varied process conditions, representing one of the most extensive and consistent experimental datasets currently available in the WAAM literature for low-carbon steel. In addition to experimental insights, this study aims to establish predictive analytical relationships for structural engineering applications, linking key input parameters with the resulting thermal cycles, deposition geometry, and mechanical properties of WAAM-fabricated steel. These correlations will serve as the foundation for process models, enabling more efficient parameter selection, automated slicing, and property-aware design of WAAM

structural components.

2. Materials and methods

2.1. Methods

This study followed a three-stage experimental approach, schematically represented in Fig. 1, to investigate the effects of WAAM process parameters on deposition quality, microstructure, and mechanical performance.

The first stage aimed to develop a broad process parameter window using the CMT mode. The objective of Stage 1 was to define the process window boundaries by systematically varying the welding current, voltage, and travel speed. This approach enabled the assessment of deposition stability, bead regularity, and defect formation across a wide range of processing conditions. Specifically, the welding current was varied between 60 and 300 A, the voltage between 11.5 and 18.5 V, and the travel speed between 8 and 18 mm/s. Ten-layer single-bead walls were manufactured under each condition to identify stable versus unstable deposition regimes and the corresponding geometrical responses. The detailed process parameters used in Stage 1 are summarised in Table 2. In the table, the heat input (HI) for each condition was calculated according to [39]:

$$HI = \frac{Current \times Voltage}{Travel\ speed} \quad \text{Eq. 1}$$

Based on the findings from Stage 1, a second experimental phase was conducted to examine the microstructural and geometrical characteristics of WAAM walls. In this stage, ten-layer single-bead walls were produced using three metal transfer modes: CMT, P-GMAW and S-GMAW. Parameter sets for Stage 2 were selected based on Stage 1 findings to span representative conditions across the identified stability window, including low, medium, and high heat input regimes. The selected process conditions are detailed in Tables 3–5. For each wall, a comprehensive set of analyses was performed. Thermal cycles were recorded using a FLIR A600-series infrared thermographic camera positioned at an average distance of 500 mm from the wall, with an emissivity value of 0.65 applied for temperature calibration. The $\Delta t_{8/5}$ cooling time, representing the time to cool from 800 °C to 500 °C, was extracted to characterise the thermal history of the deposition process, following the procedures and recommendations outlined in [40]. This system also allowed the real-time monitoring and control of the interpass temperature, which was always maintained below 250 °C. The geometry of each deposited layer was captured using a Garmo GarLine laser profilometer, and a custom-developed Python script was used to calculate the evolution of bead width and wall height with each successive layer. For metallographic analysis, cross-sections were taken from the mid-length of selected walls and prepared according to ASTM E3–01 [41] for optical microscopy. Transverse specimens were cut from all walls, cold-mounted, polished, etched with 2 % Nital, and observed using a Leica DM4000 M LED optical microscope. Finally, Vickers microhardness measurements were performed on the same samples using a Shimadzu Microhardness Tester with a 0.5 kgf load. Indentations were spaced at 0.5 mm intervals vertically along the build direction and horizontally across the wall width.

In the third and final stage of the investigation, full-scale WAAM

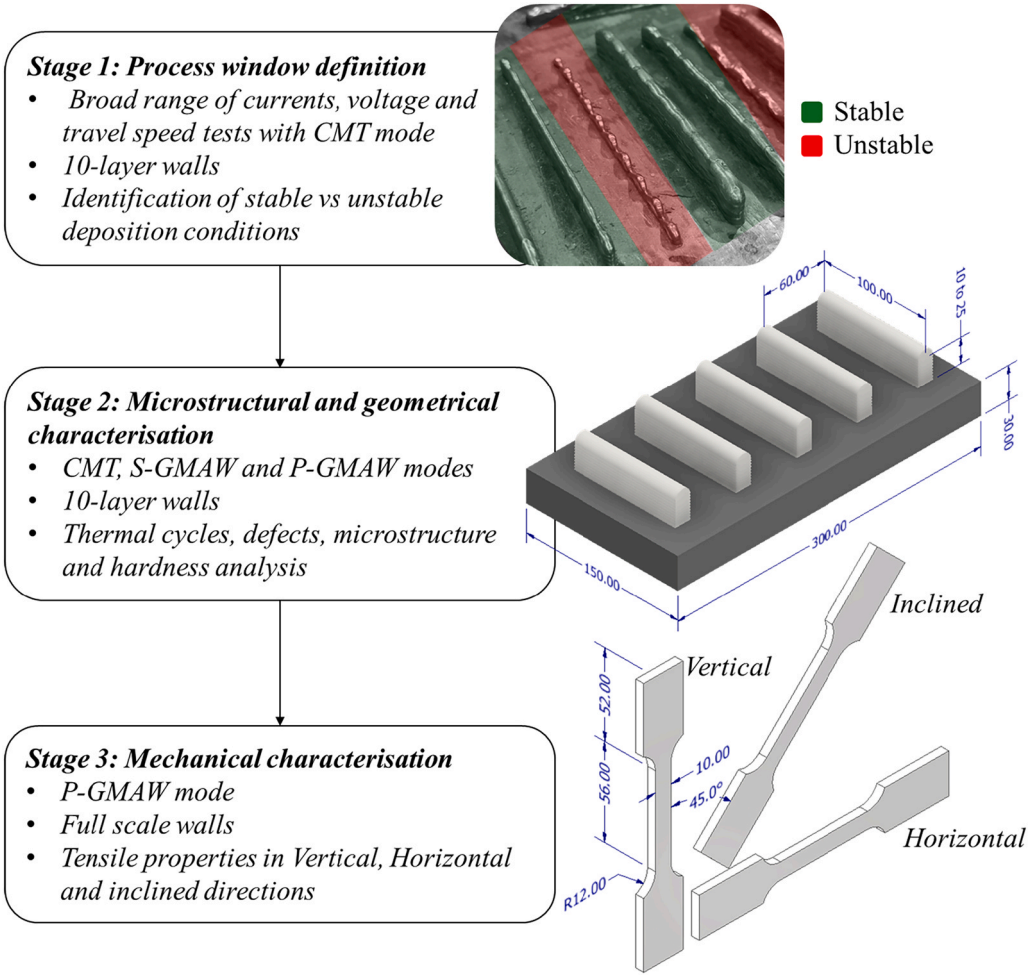

Fig. 1. Schematic overview of the three-stage experimental methodology.

Table 2
Process parameters used in Stage 1 of the experimental program for the CMT deposition mode.

Test number	Process	Current A	Travel speed mm/s	Voltage V	Wire Feed Speed m/min	Heat Input kJ/mm
1	CMT	60	8	11.5	2.3	0.09
2		60	13	11.5	2.3	0.05
3		110	8	13.2	3.1	0.18
4		110	13	13.2	3.1	0.11
5		159	8	15.2	4.3	0.30
6		300	8	18.5	10.3	0.69
7		252	8	16.7	7.6	0.53
8		159	10.5	15.2	4.3	0.23
9		200	8	15.8	5.5	0.40
10		200	10.5	15.8	5.5	0.30
11		252	10.5	16.7	7.6	0.40
12		300	10.5	18.5	10.3	0.53
13		134	11.75	14.1	3.6	0.16
14		159	13	15.2	4.3	0.19
15		200	13	15.8	5.5	0.24
16		252	13	16.7	7.6	0.32
17		252	15.5	16.7	7.6	0.27
18		300	13	18.5	10.3	0.43
19		300	15.5	18.5	10.3	0.36
20		200	15.5	15.8	5.5	0.20
21		60	18	11.5	2.3	0.04
22		110	18	13.2	3.1	0.08
23		159	18	15.2	4.3	0.13
24		200	18	15.8	5.5	0.18
25		200	18	15.8	5.5	0.18
26		300	18	18.5	10.3	0.31
27		252	18	16.7	7.6	0.23
28		60	15.5	11.5	2.3	0.04
29		110	15.5	13.2	3.1	0.09
30		60	14.25	11.5	2.3	0.05

Table 3
Process parameters for Stage 2 of the experimental programme: CMT mode.

Test number	Process	Current A	Travel speed mm/s	Voltage V	Wire Feed Speed m/min	Heat Input kJ/mm
CMT_1	CMT	100	11.5	12.8	2.6	0.11
CMT_2		141	16.5	14.4	3.9	0.12
CMT_3		141	16.5	14.4	3.9	0.12
CMT_4		200	20	15.8	5.7	0.16
CMT_5		260	16.5	16.9	7.8	0.27
CMT_6		260	16.5	16.9	7.8	0.27
CMT_7		200	11.5	15.8	5.7	0.27
CMT_8		200	11.5	15.8	5.7	0.27
CMT_9		200	11.5	15.8	5.7	0.27
CMT_10		141	6.5	14.4	3.9	0.31
CMT_11		141	6.5	14.4	3.9	0.31
CMT_12		300	11.5	16.7	10.6	0.44
CMT_13		260	6.5	16.9	7.8	0.68
CMT_14		260	6.5	16.9	7.8	0.68
CMT_15		200	3	15.8	5.7	1.05

walls with dimensions of approximately 355 × 190 mm were fabricated exclusively using the P-GMAW mode to evaluate the mechanical performance of components produced under conditions representative of industrial-scale applications. Parameter sets were selected based on the experimental findings from Stages 1 and 2 of the present study, resulting in specimens with varying thicknesses and deposition conditions. Table 6 summarises the deposition parameters employed in this stage. The goal of this stage was to establish a mechanical property–process map that links input parameters to resulting tensile behaviour. For this purpose, material coupons for uniaxial tensile testing were extracted from each wall in three different orientations using CNC machining: vertically, parallel to the build direction and normal to the substrate; horizontally, parallel to the deposition path and perpendicular to the build direction; and at an inclined angle of 45° relative to the build

Table 4
Process parameters for Stage 2 of the experimental programme: S-GMAW mode.

Test number	Process	Current A	Travel speed mm/s	Voltage V	Wire Feed Speed m/min	Heat Input kJ/mm
S-GMAW_1	S-GMAW	102	11.5	16.8	2.6	0.15
S-GMAW_2		196	20	20.1	5.9	0.20
S-GMAW_3		196	11.5	20.1	5.9	0.34
S-GMAW_4		196	7.5	20.1	5.9	0.53
S-GMAW_5		150	5	17.8	4	0.53
S-GMAW_6		300	11.5	28	10	0.73
S-GMAW_7		250	7.5	26.5	7.8	0.88
S-GMAW_8		140	2.5	17.4	3.7	0.97
S-GMAW_9		160	2.5	18.3	4.4	1.17
S-GMAW_10		240	5	24.4	7.6	1.17
S-GMAW_11		196	3	20.1	5.9	1.31
S-GMAW_12		265	5	24.4	8.5	1.29

direction. All specimens were carefully machined to eliminate surface waviness and irregularities, ensuring that the measured tensile response reflected intrinsic material properties. Tensile tests were performed using a 250 kN Shimadzu AGS-V2 universal testing machine equipped with a mechanical MFA Mess- & Feinwerktechnik GmbH extensometer in accordance with ISO 6892 [42] (Method B). Key mechanical metrics, including yield strength, ultimate tensile strength and ductility were evaluated as functions of both build orientation and processing conditions.

2.2. Materials

In all stages, WAAM walls were fabricated at the Additive Manufacturing Laboratory of the University of Coimbra using an ABB IRB 4600 six-axis robotic arm integrated with a Fronius TPS 400i CMT welding system. A 1.2 mm AM46 (AWS ER70S-6 equivalent) welding wire supplied by Böhler Voestalpine was used as the feedstock material. This solid wire was specifically developed for WAAM of cryogenic fine-grained steel structures. The weld beads were deposited onto substrate plates composed of S460 ML structural steel, selected for its mechanical compatibility with the feedstock. The chemical compositions of both materials, as supplied by the manufacturer, are listed in Table 7, and their corresponding nominal mechanical properties are summarized in Table 8. The used shielding was the M21 gas mixture consisting of 82 % Argon and 18 % CO_2, with a constant flow rate of 20 L/min during deposition.

3. Results and discussion

3.1. Stage 1: WAAM process window

This section presents the main findings from Stage 1, following the three-stage methodology outlined in Fig. 1. The process stability of each parameter set was assessed through visual inspection of the deposited walls. Stable and continuous bead formation, and uniform layer were used as primary indicators of acceptable process conditions.

The process window map presented in Fig. 2 provides a visualisation of the conditions under which stable walls were produced using CMT. The figure shows the travel speed on the vertical axis, welding current

Table 5
Process parameters for Stage 2 of the experimental programme: P-GMAW mode.

Test number	Process	Current	Travel speed	Voltage	Wire Feed Speed	Heat Input
		A	mm/s	V	m/min	kJ/mm
P-GMAW_1	P-GMAW	60	5.5	18.3	1.8	0.20
P-GMAW_2		150	10	21.3	4.7	0.32
P-GMAW_3		200	7.5	23.8	7	0.63
P-GMAW_4		150	5	21.3	4.7	0.64
P-GMAW_5		140	2.5	21.1	4.4	1.18
P-GMAW_6		240	5	25.2	7.9	1.21
P-GMAW_7		200	3	23.8	7	1.59

Table 6
Welding parameters used in Stage 3 of the experimental programme for the fabrication of full-scale WAAM walls for tensile testing.

Test number	Process	Current	Travel speed	Voltage	Wire Feed Speed	Heat Input
		A	mm/s	V	m/min	kJ/mm
Wall_1	P-GMAW	150	9	21.3	4.37	0.36
Wall_2		60	3	18.3	1.8	0.37
Wall_3		150	6	21.3	4.37	0.53
Wall_4		300	11.5	28	10	0.71
Wall_5		140	2.5	21.1	4.4	1.18

Table 7
Chemical composition of the welding wire and substrate material (wt%).

	C	Mn	Si	S	P	Cr	Mo	Ni	Fe
AM46	0.09	1.60	0.49	0.0006	0.012	0.041	0.008	0.032	Balance
S460 ML	0.10	1.70	1.00	-	-	-	-	-	Balance

on the lower horizontal axis, and includes the wire feed speed in logarithmic scale on the upper horizontal axis. Each data point corresponds to a unique parameter combination and the quality of the produced walls was color-coded based on visual inspection of the deposited wall morphology. The green region (Fig. 2 g to i) denotes stable deposition, where continuous and geometrically uniform walls were achieved. Yellow points (Fig. 2e and f) indicate transitional regimes with partial geometric irregularities, while red points (Fig. 2a to c) represent unstable conditions where deposition failed or resulted in severe discontinuities. The macrographs in Fig. 2j to m illustrate representative examples of walls from each stability category.

The results show that stable regions on the map reveal a clear dependence on the coordination between travel speed, current and wire feed speed. Stable walls were consistently produced when the travel speed was below 10 mm/s, regardless of the current or wire feed speed used (Fig. 2g to i). For lower wire feed speeds and current values, the transition from stable walls to unstable walls is very sharp (Fig. 2a and i), indicating that stable deposition is highly sensitive to small parameter variations in this range. On the other hand, for larger wire feed speeds and current values, the tolerance for printable walls (represented by the yellow dots) is broader (Fig. 2e and f).

Successful deposition requires that the material delivered into the melt pool be volumetrically compatible with the motion of the torch along the build path, while also ensuring sufficient energy input to fully melt the filler wire and maintain a stable molten pool. When this balance is achieved, the melt pool remains consistently supplied, allowing for uniform solidification and layer buildup. For low current values, in regions where travel speed is high relative to wire feed speed (Fig. 2a to c), deposition becomes unstable. For this, insufficient filler material is introduced to match the forward motion of the torch, leading to incomplete beads. The lack of continuity and bonding between successive layers in this regime is typically associated with high porosity, interrupted fusion lines, and premature process failure. On the other hand, for high current and wire feed speed values, at high travel speeds, although complete walls can still be deposited under these conditions, the high travel speed limits the time available for the molten pool to redistribute uniformly (Fig. 2d and e). This results in inconsistent layer buildup and abrupt variations in wall thickness, typically observed in the yellow region of the process map. When the travel speed is reduced under similar wire feed and current conditions, the increased dwell time allows for better molten pool control, improving uniformity and mitigating geometric irregularities.

Table 8
Nominal mechanical properties of the welding wire and substrate material.

Feedstock wire	Yield stress (MPa)	Ultimate strength (MPa)	Elongation at fracture (%)
AM46	420	460	24
S460 ML	49	584	26

3.2. Stage 2: assessment of transfer mode and process parameters

3.2.1. Process parameters

This section assesses the combined influence of transfer mode and process parameters on the thermal cycles, bead morphology, and hardness distribution of WAAM walls. In modern welding power sources, the current, voltage and *WFS* are not independent since they follow predefined synergic process lines which select optimum process parameters. The relationships between the welding current with the arc voltage and the wire feed speed across the three metal transfer modes are represented in Fig. 3. As shown in the figure, a strong linear correlation is evident for all transfer modes, demonstrating that the *WFS* increases proportionally with the current. This is expected since the feed rate must increase with the current to maintain a consistent melt rate and droplet detachment frequency. Importantly, no significant variation is observed across transfer modes in this relationship.

In addition, a linear relationship is also observed between current and voltage across all transfer modes. The CMT mode, characterised by controlled short-circuiting and lower thermal input, consistently exhibits the lowest voltage values throughout the current range. This behaviour is expected, as CMT employs frequent wire retraction and precise droplet detachment to maintain a short arc length, thereby reducing the required arc voltage. In contrast, the S-GMAW and P-GMAW modes operate in spray or pulsed-spray regimes, which rely on

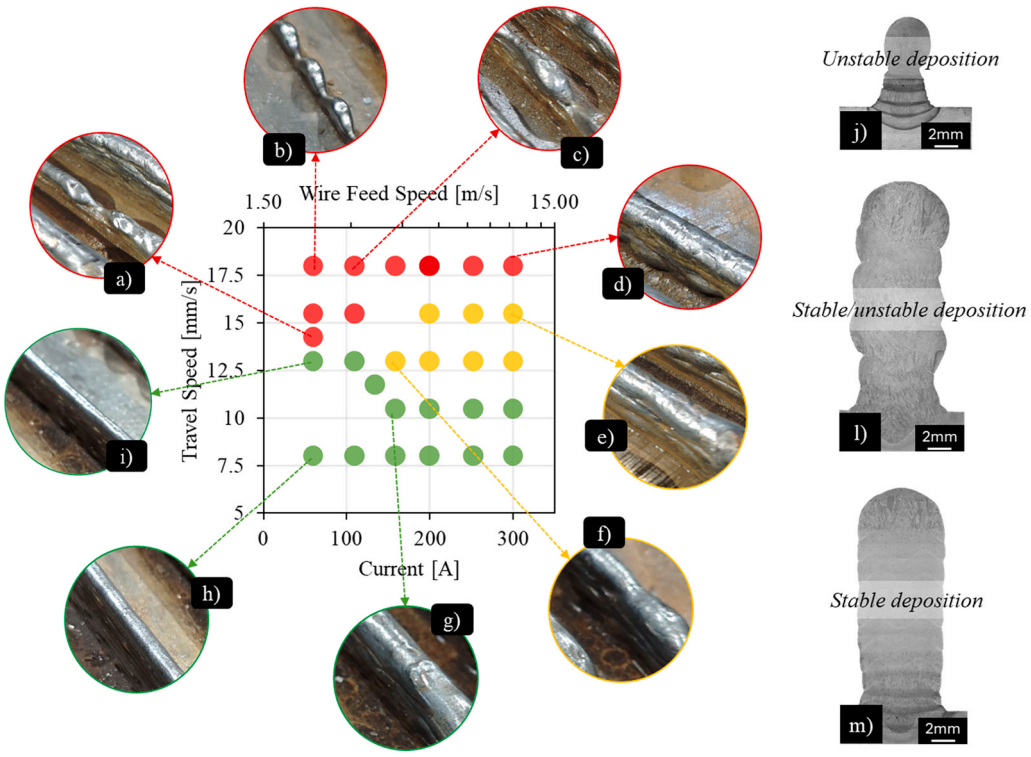

Fig. 2. Process window map for 10-layer-height walls produced using the WAAM CMT, where the quality of the walls is represented by (a to d) red dots (unstable conditions, incomplete walls), (e and f) yellow dots (printable but with large geometric variations), and (g to i) green dots (stable walls with consistent geometry). Macrographs (j to m) of representative walls for each stability category.

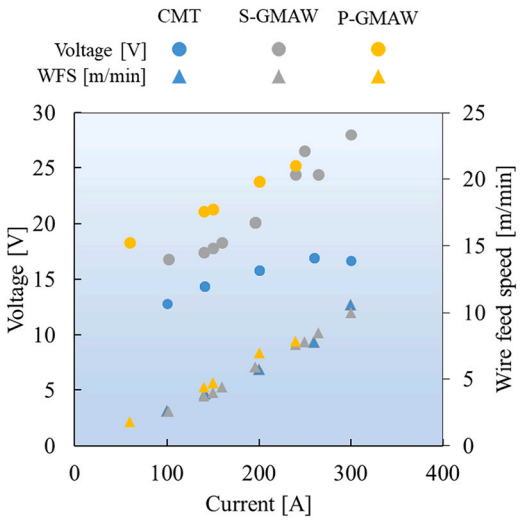

Fig. 3. Relationship between welding current with the arc voltage and wire feed speed for the three metal transfer modes investigated (CMT, S-GMAW, and P-GMAW).

stable droplet transfer. These modes require longer arc lengths to sustain such transfer mechanisms, resulting in higher arc voltages. Furthermore, at higher current levels, the arc voltages for S-GMAW and P-GMAW largely overlap. However, at lower current levels, P-GMAW often exhibits slightly higher average voltages than S-GMAW for equivalent current settings. This difference can be attributed to the nature of pulsed waveforms, which alternate between a low background current and a high peak current. The elevated average voltage arises from the contribution of these high-energy peak phases. Additionally, some power sources apply more active voltage regulation in pulsed mode to stabilise the arc and prevent extinction during the low-current base phase, further contributing to the higher average voltage observed.

3.2.2. *Thermal cycles*

Understanding the evolution of thermal cycles during WAAM is critical for predicting microstructural development and residual stress formation. One of the most informative thermal descriptors is the $\Delta t_{8/5}$ cooling time, which reflects the time required for the material to cool from 800 °C to 500 °C, a temperature range strongly associated with phase transformation kinetics in steel.

The $\Delta t_{8/5}$ is represented in Fig. 4 as a function of heat input across three characteristic layers of the WAAM-deposited walls (layers number 1, 5, and 10) for the CMT, S-GMAW and P-GMAW transfer modes. For all layers in Fig. 4, the cooling time $\Delta t_{8/5}$ increases linearly with heat input. This behaviour is consistent with fundamental thermal principles governing heat transfer in multilayer welding processes, where higher heat input results in slower cooling rates. Furthermore, the slopes of the linear fits provide additional insight into the thermal evolution of the deposition process. The increasing trend in slope values from 6.38, 16.11, and 32.47 for layers 1, 5, and 10, respectively, indicates a significant reduction in the rate of heat dissipation as the wall height increases. This observation aligns with prior research [40,43–45] on multi-pass welding and additive manufacturing, where heat accumulation leads to a thermal stabilisation effect, reducing local cooling rates. Additionally, the linear fits for all layers exhibit exceptionally high correlation coefficients ($R^2 > 0.96$), which show the strong linear relationship between heat input and cooling time.

Regardless of the specific welding process, the relationship between the $\Delta t_{8/5}$ and the heat input remains identical, indicating that the primary governing factor for cooling rate variation is the thermal energy introduced into the system rather than the metal transfer mode itself.

3.2.3. *Metallographic analysis*

To complement the thermal cycle analysis, metallographic

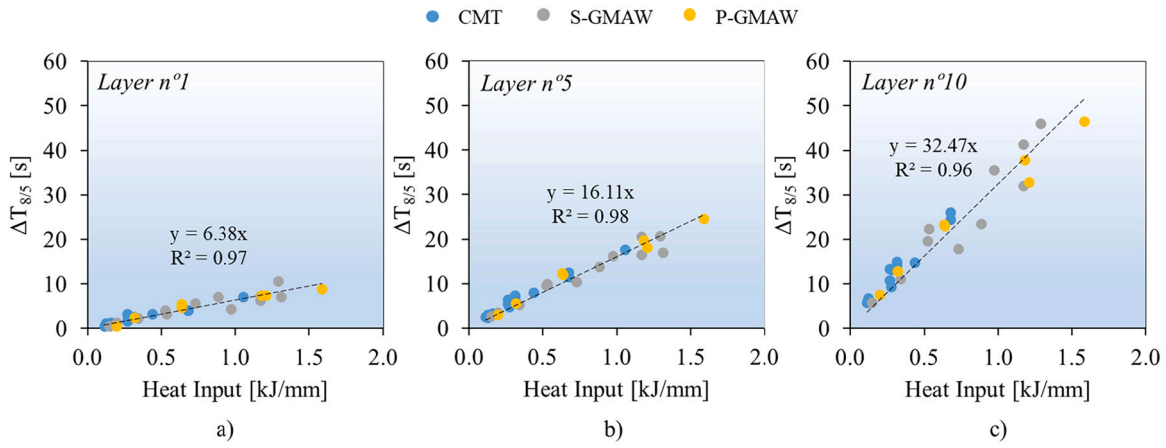

Fig. 4. $\Delta t_{8/5}$ cooling time as a function of heat input for WAAM-deposited walls using CMT, S-GMAW, and P-GMAW, at three deposition stages: layers (a) 1, (b) 5, and (c) 10.

characterisation was carried out to investigate the influence of the deposition parameters on the microstructural evolution of WAAM-deposited walls. Fig. 5 represents the macro and microstructural assessment of a wall fabricated using CMT with a current of 200 A, travel speed of 3 mm/s, voltage of 15.8 V and corresponding heat input of 1.05 kJ/mm (sample 15 of Table 3). Fig. 5a displays the macrostructure of the wall produced, while Fig. 5b to e illustrates the microstructural evolution of the HAZ, wall bottom, middle, and top parts, respectively.

Fig. 5a reveals the layered macrostructure, where each layer corresponds to the deposition trajectory of the welding torch. Analysing the microstructure of the HAZ within the substrate (Fig. 5b), a coexistence of martensite and bainite structures is evident. This occurrence arises from the regions experiencing temperatures surpassing the steel A3 temperature, coupled with rapid cooling rates facilitated by the heat dissipation through the substrate. Moving to the wall bottom region (Fig. 5c), it is possible to observe a microstructure with small grain size and some brittle phases, such as bainite. This phenomenon is again attributed to the fast cooling rates during the initial deposition pass. Analysing the microstructure of the wall middle region (Fig. 5d), it is possible to observe that the microstructure comprises polygonal ferrite and intergranular lamellar pearlite. The heat input from each pass results in partial remelting of preceding layers, accumulating heat on the deposited wall. Consequently, this accumulation leads to slower cooling rates and a coarser and ductile microstructure. Finally, by analysing the microstructure top layer of the wall (Fig. 5d), it is possible to observe a mixture of acicular ferrite, allotriomorphic ferrite and bainite. These microstructural characteristics arise since this region has not experienced the thermal effect of the following layer depositions. It should be noted that these microstructural variations between the lower and upper regions of the wall result from the transient thermal conditions typical of the initial deposition passes.

To better understand the influence of heat input on the microstructural evolution of WAAM-deposited walls, Fig. 6 presents a comparative characterisation of two samples produced using the CMT process. Both samples were extracted from the middle height of the wall. The two conditions correspond to high and low heat inputs of 1.05 kJ/mm and 0.11 kJ/mm, respectively. Fig. 6a and b show etched optical micrographs of the two samples, while Fig. 6c and d display corresponding colour-coded grain size distribution maps. The microstructure in the high heat input condition exhibits visibly coarser grains, whereas the

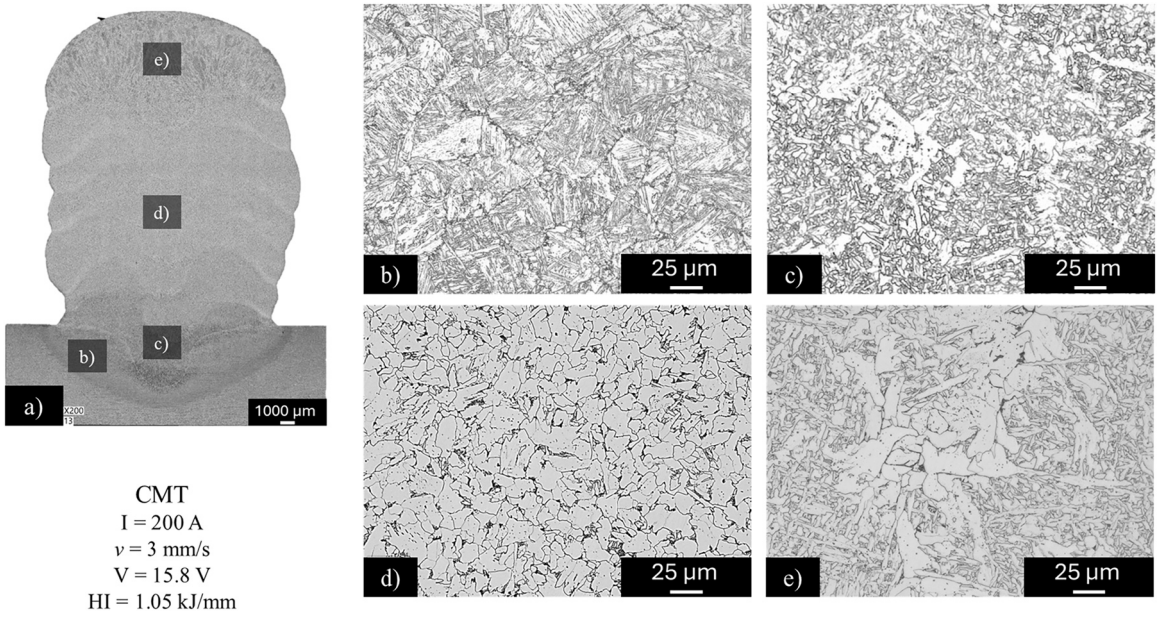

Fig. 5. Macrostructure of the (a) wall produced by CMT with a current, travel speed, voltage and heat input of 200 A, 3 mm/s, 15.8 V and 1.053 kJ/mm, respectively. Microstructure of the (b) HAZ, (c) wall bottom, (d) middle and (e) top parts.

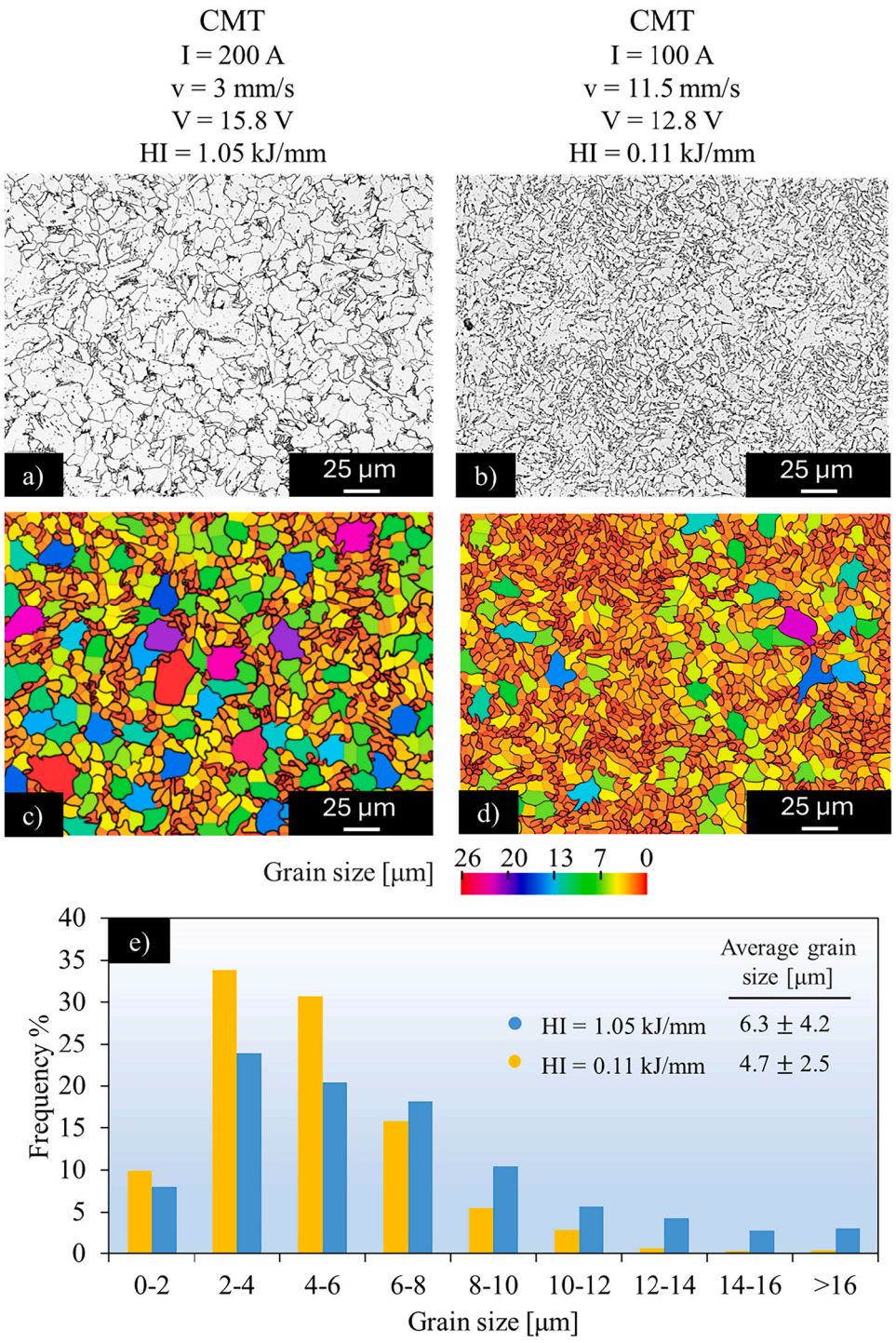

Fig. 6. Microstructural comparison at mid-wall height for CMT-WAAM walls produced with high (1.05 kJ/mm) and low (0.11 kJ/mm) heat inputs: (a, b) etched optical micrographs; (c, d) grain size distribution colour maps and (e) grain size histograms and average values.

low heat input sample presents a finer grain structure. The colour maps clearly illustrate the refinement effect associated with reduced heat input, as the low heat input condition shows a higher concentration of fine grains, uniformly distributed across the field.

Fig. 6e provides the quantitative grain size histograms and average and standard deviation grain size values for both conditions. The sample deposited at 1.05 kJ/mm exhibits a more right-skewed distribution, with a higher frequency of grains exceeding 6 µm and an average grain size of 6.3 ± 4.2 µm. In contrast, the 0.11 kJ/mm sample shows a more left-shifted distribution concentrated in the 2–5 µm range, with an average grain size of 4.7 ± 2.5 µm.

These observations are consistent with the thermal cycle trends discussed in Section 3.2.2. The higher thermal energy input leads to slower cooling rates, which promote grain boundary mobility and facilitate grain growth. Conversely, the lower heat input condition results in faster cooling, limiting grain growth and producing a finer, more homogeneous microstructure.

The influence of metal transfer mode on microstructural features is presented in Fig. 7, which compares WAAM walls deposited using CMT, S-GMAW, and P-GMAW under similar heat input conditions. All samples

were extracted from the middle height of the wall, representing a region of thermal stability. Fig. 7a to c show the etched optical micrographs for CMT, S-GMAW, and P-GMAW, respectively. Fig. 7d to 7f display the corresponding colour-coded grain size distribution maps, and Fig. 7g presents the grain size histograms along with the average and standard deviation values for each metal transfer mode.

Despite the distinct arc behaviours and droplet transfer mechanisms associated with each process, the resulting microstructures are remarkably similar. All three conditions exhibit phase morphologies dominated by polygonal ferrite and intergranular lamellar pearlite. This consistency indicates that, when heat input is maintained constant, the cooling rate and thermal gradients are the primary factors governing grain transformation and morphology.

The grain boundary mapping and histogram analyses further support this conclusion. In all three cases, the microstructures show a predominance of fine to medium grain sizes, while larger grains are relatively scarce and uniformly distributed. The measured average grain sizes are 6.3 ± 4.2 μm for CMT, 6.4 ± 3.8 μm for S-GMAW, and 6.8 ± 3.5 μm for P-GMAW, indicating negligible variation across transfer modes. The overlapping histogram distributions reinforce the finding that the metal transfer mode has a secondary influence on grain morphology in the mid-wall region, provided the heat input remains equivalent.

3.2.4. Wall geometry

In manufacturing processes, and particularly in WAAM, the geometric accuracy and consistency of the deposited wall are critical to achieving high-quality components with minimal post-processing. Key geometric parameters such as layer width and height are directly influenced by the process parameters. Understanding the relationship between process conditions and wall geometry is essential for defining slicing strategies, which define the interlayer height and torch path for each layer.

This section investigates the influence of transfer mode and deposition parameters on the evolution of wall geometry during multilayer deposition. Special attention is given to the layer width and height evolution with the build direction, as cumulative thermal and mechanical effects may introduce deviations from ideal layer stacking.

Fig. 8 shows the relationship between layer width with the

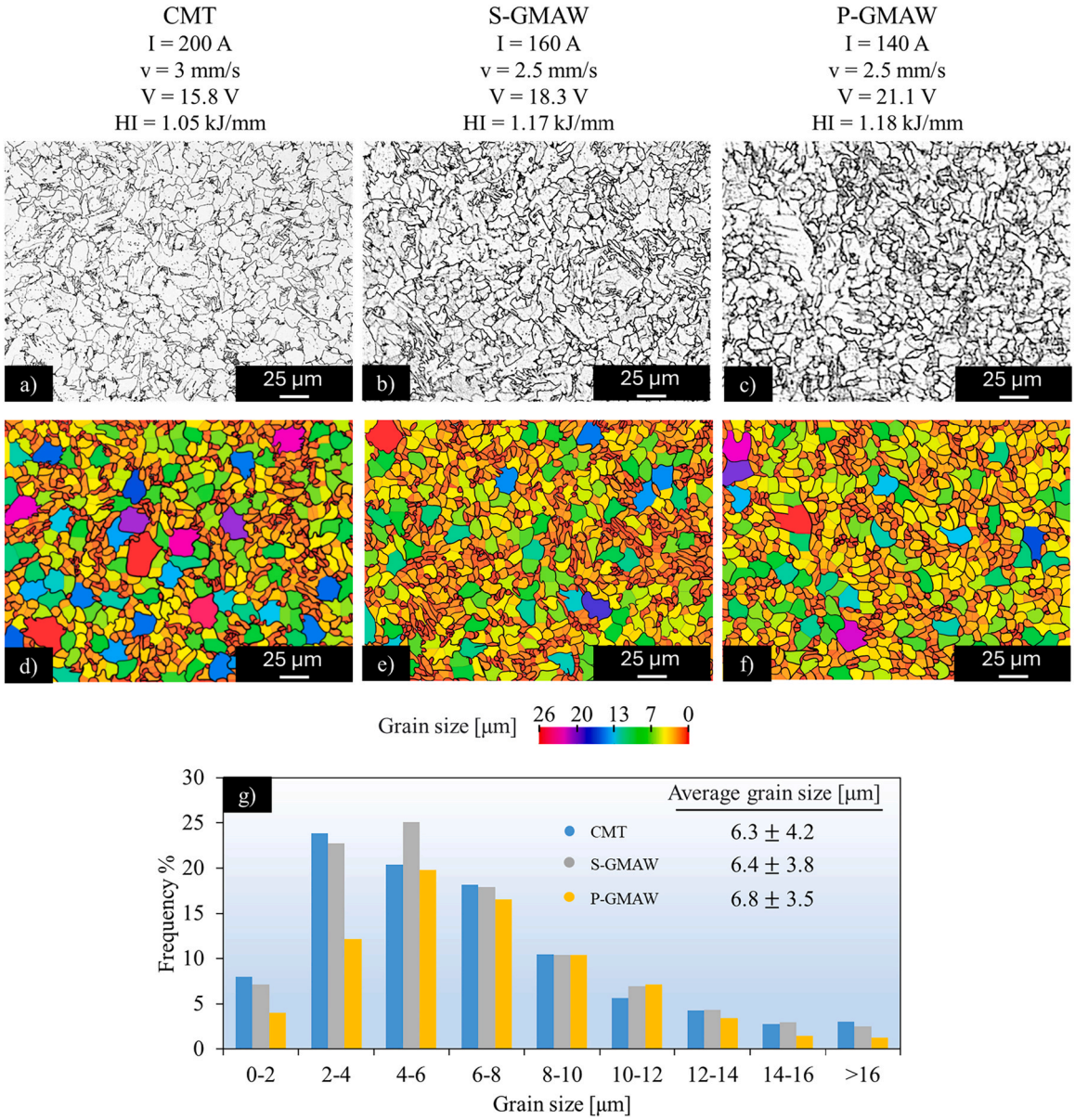

Fig. 7. Microstructural comparison at mid-wall height for WAAM samples produced using CMT, S-GMAW, and P-GMAW at similar heat input. (a–c) Optical micrographs; (d–f) grain size distribution colour maps and (g) grain size histograms and average values.

coefficient defined as the product of the wire feed speed to travel speed ratio (*WFS/TS*), where both WFS and TS are expressed in mm/s, and the heat input (*HI*), for three representative deposition layers, layer 1, layer 5 and layer 10, using the CMT, S-GMAW, and P-GMAW metal transfer modes. This coefficient integrates two critical physical aspects of the WAAM process, i.e. the material deposition rate per unit length and the thermal energy input. The first governs the volumetric flow of material deposited along the build path, while the second affects the melt pool dynamics and wettability, which controls the lateral spreading of the deposited bead. By combining these factors, the composite index provides a more holistic descriptor of the conditions shaping bead geometry.

The results demonstrate a clear power-law dependency between the proposed coefficient and the measured bead width for layers 1, 5, and 10, with high correlation coefficients (R^2 =0.89, R^2 =0.96 and R^2 =0.98, respectively), which shows that the combined influence of deposition rate and energy input effectively governs the bead width. The exponents of the fitted curves remain consistent across the three layers, indicating that the bead width remained almost constant throughout the wall.

The data also indicate that the metal transfer mode does not exhibit any significant influence on bead width under comparable deposition conditions, as evidenced by the overlapping data trends for CMT, S-GMAW, and P-GMAW in all layers.

To correlate the evolution of layer height in relation to fundamental process parameters, a composite index was formulated by combining the square root of the wire feed speed to travel speed ratio ($\sqrt{WFS/TS}$) with heat input raised to a reduced exponent ($HI^{-0.2}$). These indices were selected to reflect the dominant role of material deposition rate in determining layer buildup, while still capturing the secondary influence of the thermal energy. The exponent applied to *HI* was empirically optimised to improve correlation with the experimental height measurements. Fig. 9 illustrates the relationship between this coefficient and the layer height for three deposition stages, at layers 1, 5, and 10, and for all metal transfer modes tested. It is concluded that a power-law relationship across all layers, results in coefficients of determination R^2 = 0.94, R^2 = 0.84 and R^2 = 0.92, respectively.

Comparing the layer height for the different layers, it is possible to observe a gradual decrease in both the power-law exponent and the scaling factor, indicating a slightly diminishing sensitivity of layer height for the upper layers. In the initial layers, the cold substrate promotes efficient solidification, resulting into vertical growth. In contrast, upper layers experience accumulated heat and partial remelting, which reduces the net layer height per pass, despite similar input parameters.

The effect of the metal transfer mode on the results shows no significant deviation across CMT, S-GMAW, and P-GMAW processes. Data points from all transfer modes fall along the same fitted trendlines, suggesting that under comparable deposition conditions, the transfer models do not play a primary role in determining the final layer height.

3.2.5. Hardness

This section presents the mechanical characterisation of WAAM-deposited steel walls, focusing on microhardness distribution. Hardness testing was performed on cross-sections extracted from representative walls using different transfer modes and process parameters to assess the local mechanical properties of the printing parameters.

As an example, Fig. 10 presents both vertical and horizontal Vickers hardness profiles for a WAAM wall deposited using the CMT process with a current, traverse speed, voltage, and heat input of 141 A, 6.5 mm/s, 16.9 V, and 0.312 kJ/mm, respectively. The horizontal profile was performed along a line located 0.5 mm above the substrate surface, targeting the HAZ, while the vertical profile was acquired along the central axis of the wall, extending from the substrate interface to the topmost deposited layer. All hardness measurements were taken at intervals of 0.5 mm. Four distinct regions are highlighted in the figure, identifying the top, middle, and bottom sections of the deposited wall, as well as the HAZ within the substrate.

The horizontal profile shows that the hardness values within the HAZ are consistently higher than those of the substrate. As the measurement line approaches the fusion boundary, the hardness increases progressively, reaching its peak near the interface between the HAZ and the fusion zone. This localised hardening is attributed to the rapid cooling and phase transformation in the substrate-adjacent regions. Within the fusion zone itself, the hardness values are slightly lower than those observed at the HAZ-fusion boundary, however they remain elevated compared to the substrate baseline. The vertical hardness profile provides further insight into the mechanical evolution across the wall height. In the bottom region of the deposited wall, hardness values are initially high, then gradually decrease toward the mid-section. Above the midpoint, hardness values stabilise and remain relatively uniform until the uppermost layers, where a secondary increase in hardness is observed.

This evolution in hardness profile was consistent across all analysed WAAM walls, regardless of the specific metal transfer mode employed. The increased hardness observed in the substrate, HAZ, and lower wall sections is linked to faster cooling rates in these regions, which promote the formation of harder, brittle microstructures such as martensite and bainite. In contrast, the mid-wall zone is subject to repeated thermal cycles and heat accumulation, resulting in slower cooling rates and the formation of softer phases like polygonal ferrite and intergranular lamellar pearlite. The hardness increase at the wall top is explained by

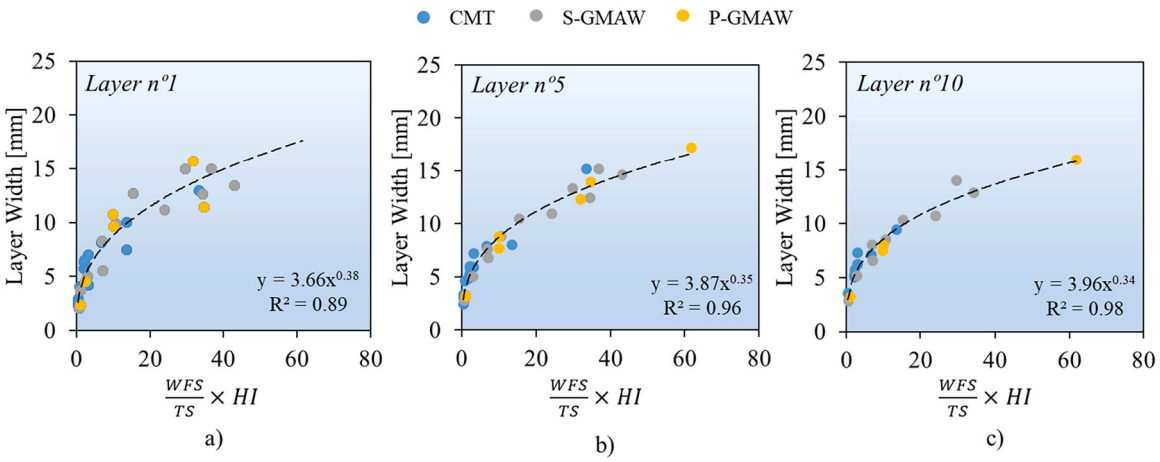

Fig. 8. Evolution of the layer width as function of a coefficient defined as the product of the wire feed speed to travel speed ratio (*WFS/TS*) and the heat input (*HI*) for WAAM-deposited walls using CMT, S-GMAW, and P-GMAW, at three deposition stages: layers (a) 1, (b) 5, and (c) 10.

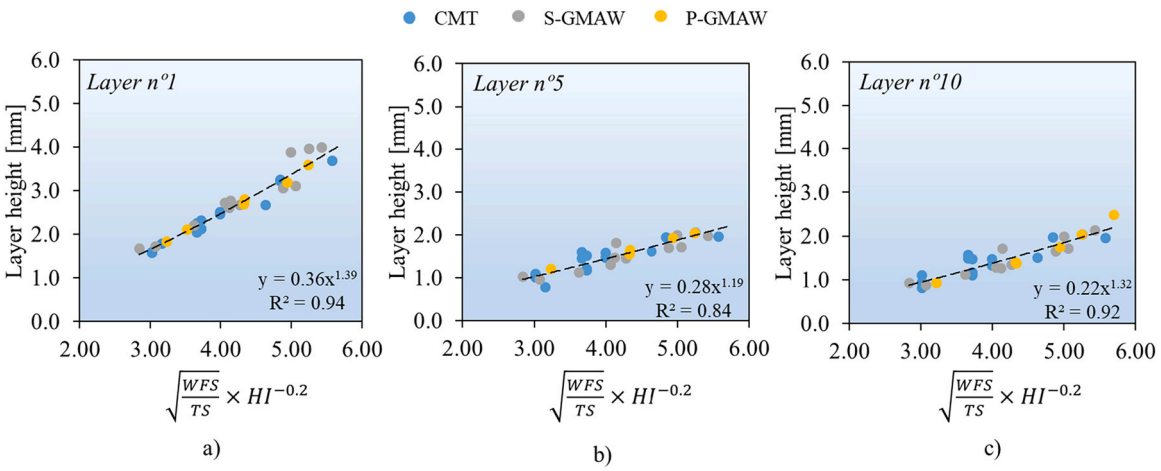

Fig. 9. Evolution of the layer height as a function of a coefficient defined as the product of the square root of the wire feed speed to travel speed ratio ($\sqrt{WFS/TS}$) and the heat input ($HI^{-0.2}$) for WAAM-deposited walls using CMT, S-GMAW, and P-GMAW, at three deposition stages: layers (a) 1, (b) 5, and (c) 10.

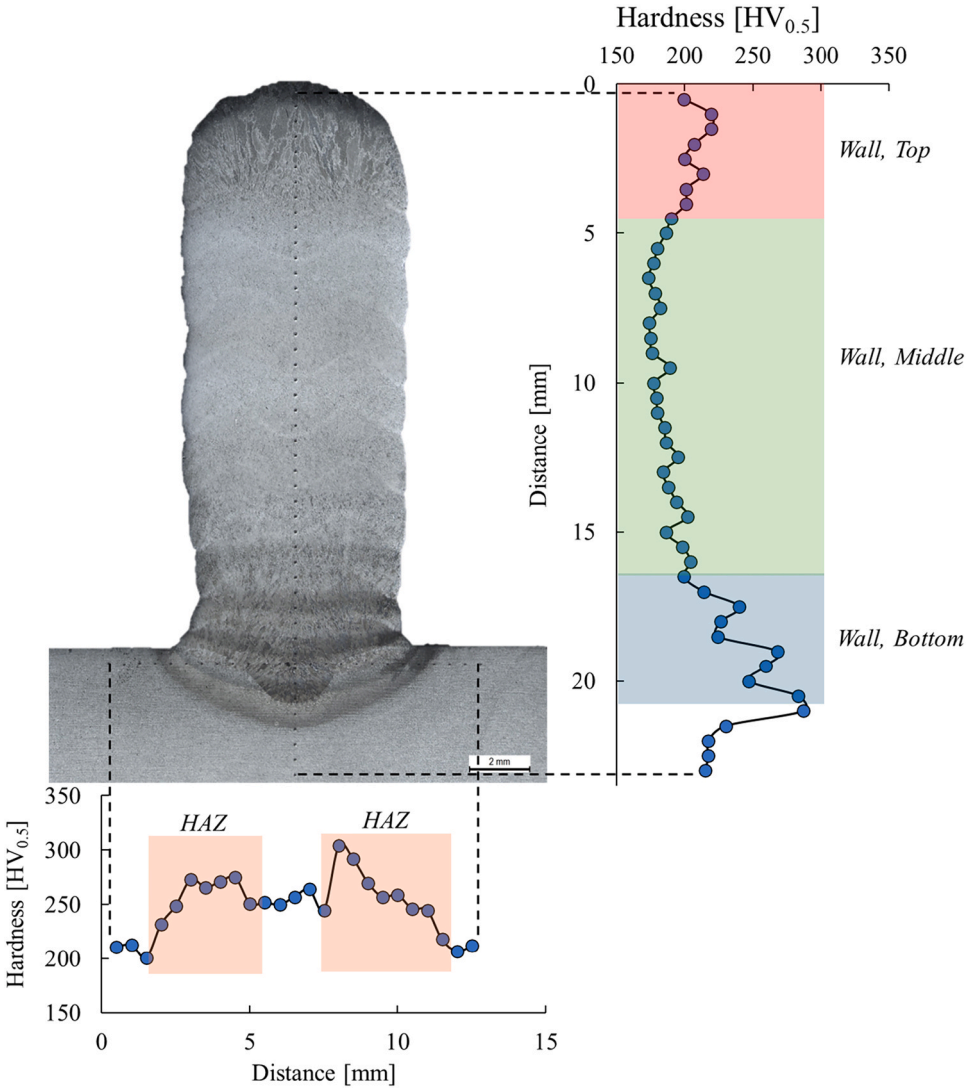

Fig. 10. Vertical and horizontal hardness profiles for the wall produced with the CMT process with a current, traverse speed, voltage, and heat input of 141 A, 6.5 mm/s, 16.9 V, and 0.312 kJ/mm, respectively.

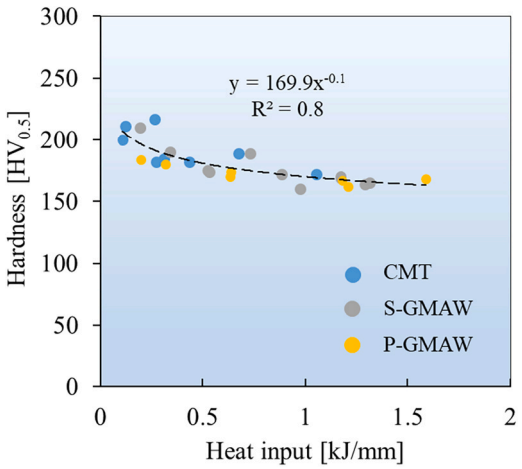

Fig. 11. Evolution of the average hardness in WAAM walls as a function of heat input for CMT, S-GMAW, and P-GMAW transfer modes.

the limited thermal exposure during deposition, favouring a more refined and untempered microstructure.

To quantify the influence of process parameters on local mechanical response, Fig. 11 represents the relationship between heat input and the average hardness values measured in the middle region of the WAAM walls. These values were calculated by averaging the hardness data corresponding to the green zone, as previously defined in Fig. 10.

As can be seen in the figure, a clear inverse trend is observed between heat input and average hardness, following a power-law decay, which indicates that higher heat input leads to progressively lower hardness values, consistent with the thermal softening and microstructural coarsening typically observed under slower cooling conditions. Moreover, the data reveal that the type of metal transfer mode has minimal influence on the resulting hardness within the wall. All three processes exhibit similar trends and closely overlapping data, reinforcing the conclusion that heat input and the resulting thermal cycles are the dominant factors governing hardness evolution, rather than the specific arc transfer dynamics.

3.3. Stage 3: mechanical properties of WAAM Walls

To complement the hardness analysis and provide a broader understanding of the mechanical performance of WAAM-fabricated structures, uniaxial tensile tests were conducted on specimens extracted from full-scale walls. These tests aimed to evaluate the influence of process conditions on key mechanical properties such as the yield strength (f_y), ultimate tensile strength (f_u), and ultimate strain (ε_u). All tensile tests were performed on walls produced using the P-GMAW transfer mode. P-GMAW was selected as universal mode available across different welding sources in compliance with the results from previous sections, which concluded on the similarity of the transfer modes for comparable heat inputs.

Fig. 12 presents the engineering stress-strain curves obtained from uniaxial tensile tests conducted on specimens extracted from P-GMAW walls fabricated under five different sets of process parameters (Fig. 12a to e). For each condition, three specimen orientations were tested, as schematically depicted in Fig. 12 f. Although three specimens were tested for each orientation, only one representative curve per direction is shown in the graphics.

The stress-strain curves showed that regardless of the specific heat input or process configuration, all samples exhibited a mechanical behaviour typical of hot-rolled structural carbon steels. The curves display well-defined regions, including an initial linear elastic region, followed by a yielding plateau, indicative of Lüders band propagation, and a strain hardening phase. Importantly, across all tested conditions, the material exhibited isotropic mechanical properties. No significant differences were observed between the vertical, horizontal, and inclined specimens within each parameter set. The near-overlapping curves across orientations indicate that the layered deposition inherent to WAAM did not introduce notable directional dependency in tensile

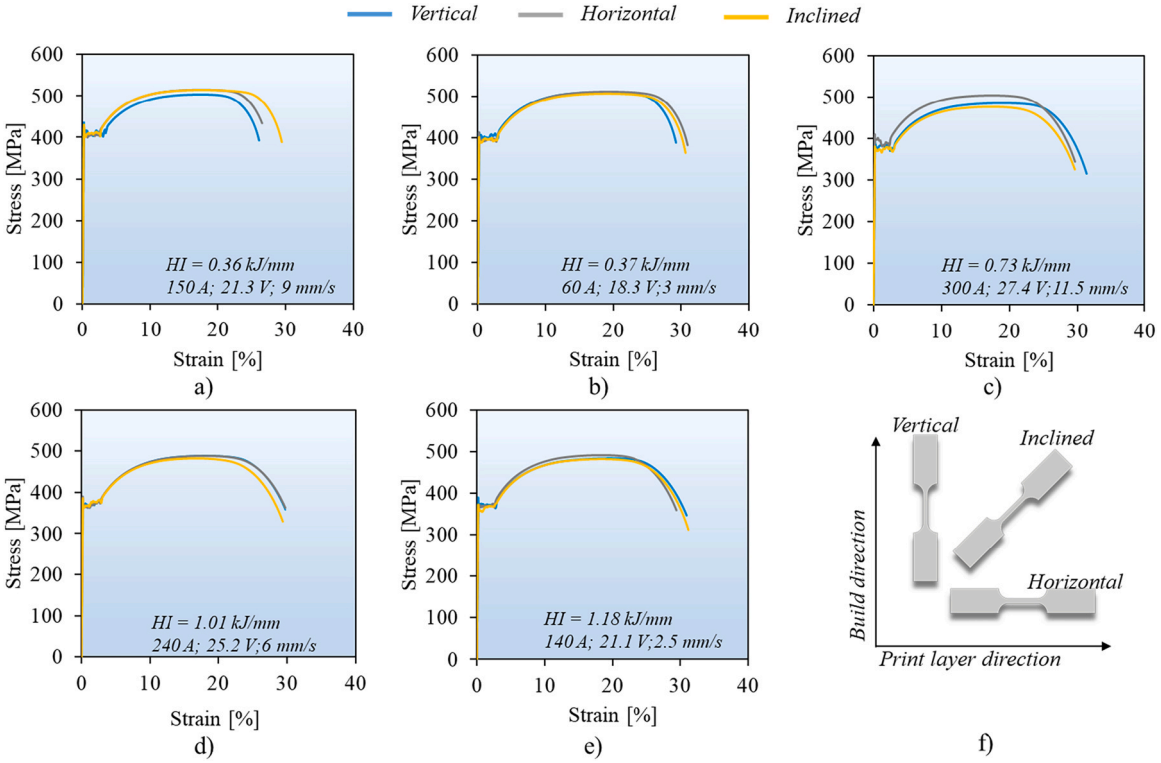

Fig. 12. Engineering stress-strain curves from P-WAAM walls produced with five process conditions (a–e), for horizontal, vertical, and inclined directions (f).

Table 9
Average tensile properties of P-GMAW coupons processed under different heat input conditions, including Young's modulus (E), yield strength (f_y), ultimate tensile strength (f_u), and ultimate strain (ε_u), for vertical, horizontal, and inclined orientations.

Heat input [kJ/mm]	Current [A]	Voltage [V]	Orientation	E [GPa]	f_y [MPa]	f_u [MPa]	ε_u [%]	f_u/f_y
0.37	60	18.3	Vertical	193.1	395.8	504.0	17.7	1.27
			Horizontal	206.1	404.8	519.7	19.0	1.28
			Inclined	202.3	388.9	504.1	18.3	1.30
0.36	150	21.3	Vertical	219.4	413.9	504.0	17.9	1.22
			Horizontal	212.1	408.2	516.4	16.8	1.27
			Inclined	197.5	404.9	510.4	17.4	1.26
0.71	300	27.4	Vertical	179.6	376.7	487.9	17.6	1.30
			Horizontal	181.0	391.9	496.3	18.6	1.27
			Inclined	184.2	373.5	481.8	18.7	1.29
1.18	140	21.1	Vertical	187.4	377.9	499.8	19.0	1.32
			Horizontal	181.2	369.4	494.1	19.3	1.34
			Inclined	186.3	362.9	481.7	18.5	1.33
1.01	240	25.2	Vertical	181.3	379.3	488.4	18.6	1.29
			Horizontal	181.2	373.3	492.0	18.2	1.32
			Inclined	181.8	370.7	485.4	18.6	1.31
Global average			**mean**	191.6	386.1	497.7	18.3	1.29
			cov	6.7 %	4.2 %	2.4 %	3.8 %	2.4 %

performance.

The average tensile properties obtained from the tested samples are summarised in Table 9, including the Young's modulus (E), yield strength, ultimate tensile strength, and ultimate strain for each build orientation and process condition. Across all heat input levels, the variation in mechanical properties with the printing direction remains relatively low, confirming the mechanical isotropic behaviour observed in the stress-strain curves of Fig. 12. The anisotropy in yield strength, ultimate tensile strength, and ultimate strain remains low in all cases, with maximum deviations below 5 % for strength parameters and not exceeding 6 % for ductility. The Young's modulus exhibits slightly higher variability, particularly for the sample produced with a heat input of 0.36 kJ/mm, registering a maximum variability of 10 %, which may be attributed to the local stiffness variations induced by thermal gradients. Overall, the small degree of anisotropy across all tensile parameters suggests that the observed variations are more likely related to localised microstructural heterogeneities than to systematic directional dependence.

Furthermore, in accordance with EN 1993–1–1 [46], structural steels must satisfy key ductility criteria to ensure adequate performance under loading. These requirements include a tensile-to-yield strength ratio $f_u/f_y > 1.1$ and a minimum elongation at fracture $\varepsilon_f > 15$ %. According to Table 9 the f_u/f_y ratios ranged from approximately 1.22–1.34, confirming compliance with the strength ratio requirement. Although the reported values correspond to the ultimate strain rather than the total fracture elongation, they consistently exceed 15 %, thereby satisfying the ductility requirement. Additionally, based on the yield strength values ranging between 360 MPa and 414 MPa, and ultimate tensile strengths between 482 MPa and 520 MPa, the mechanical behaviour of the WAAM-produced steel aligns most closely with the specifications of S355 structural steel. However, the overstrength requirements of Annex E of EN 1993–1–1 are not fulfilled for the average values of yield stress and ultimate strength ($f_{y,av} = 386.1 < 1.2 \times 355 = 426$, $f_{y,cov} = 4.2x\% < 5$ %, $f_{u,av} = 497.7 < 1.15 \times 490 = 563.5$, $f_{u,cov} = 2.4$ % < 4 %).

Fig. 13 shows the evolution of the average mechanical properties, yield strength, ultimate tensile strength, ultimate strain and Young's modulus, as a function of heat input for the produced walls. The data represent the mean values across all tested build orientations for each heat input level, with error bars indicating the corresponding standard deviations.

The yield strength and the ultimate tensile strength gradually decrease with the increasing heat input. The reduction in mechanical properties is consistent with the thermal-metallurgical effects discussed in earlier sections, particularly the observed increase in the $\Delta t_{8/5}$ cooling time. Longer thermal cycles promote microstructural coarsening,

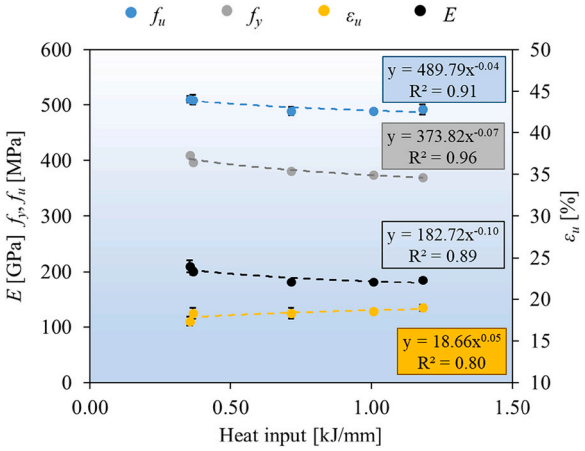

Fig. 13. Evolution of average mechanical properties: yield strength (f_y), ultimate tensile strength (f_u), ultimate strain (ε_u), and Young's modulus (E)) with the heat input for WAAM walls produced using the P-GMAW process.

weakening material resistance to plastic deformation. Both f_y, and f_u follow a power-law relationship with heat input, as evidenced by the high correlation coefficients ($R^2 = 0.96$ and 0.91, respectively). Similarly, the Young's modulus also shows a slight decrease with increasing heat input. Despite the increased data scatter at lower heat inputs, a declining power-law fit is still obtained with a reasonable correlation ($R^2 = 0.80$).

Conversely, the ultimate strain increases with heat input, indicating improved ductility. This behaviour aligns with the slower cooling rates and increased thermal accumulation in high heat input conditions, favouring the development of coarser microstructures. The evolution of ε_u with heat input is also well captured by a power-law model ($R^2 = 0.80$), which shows the influence of the thermal cycles across all key mechanical parameters.

To benchmark the tensile performance of the WAAM-fabricated AM46 walls, Fig. 14 presents the average f_y, and f_u obtained in this study with values reported in the literature for low-carbon steel WAAM components, as summarised in Table 1. According to the figure it is possible to observe that the literature dataset is predominantly concentrated in the lower heat input range, where greater scatter in the reported results is evident. This variability is likely attributable to differences in experimental setups, including interpass temperature control, deposition and cooling strategies, welding wire batch, substrate thickness, and other process-specific factors. Despite this scatter, the

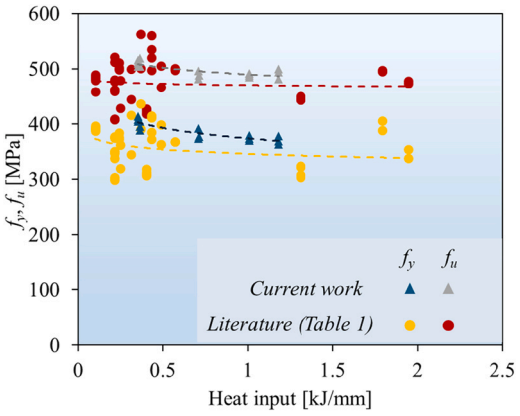

Fig. 14. Comparison of yield strength f_y, and ultimate tensile strength f_u obtained in the current work with values reported in the literature (Table 1) for AM46 (ER70S-6) WAAM components. Dashed lines indicate the trend lines for each dataset.

average trend lines in the figure indicate a consistent reduction in both f_y, and f_u with increasing heat input, which aligns well with the trends observed in the present work. Furthermore, the f_y, and f_u values obtained in this study fall within the upper segment of the range reported in the literature, and in several instances surpass it, even when compared with works employing different feedstock compositions, deposition strategies, and process parameters. These results confirm that the combination of AM46 feedstock and the selected P-GMAW process parameters provides a robust processing route for achieving consistent, high-strength WAAM components that meet structural-grade requirements.

To further characterize the tensile behaviour of the WAAM-fabricated walls and facilitate the integration of advanced analytical and numerical modelling into structural engineering applications, the bilinear plus nonlinear hardening model proposed by Yun and Gardner [47] for hot-rolled steels was considered. This constitutive model is particularly well-suited to capturing the yielding plateau and the gradual reduction in stiffness observed in the strain-hardening regime, a characteristic feature of structural steels whose applicability to additively manufactured materials requires verification. The stress–strain response $f(\varepsilon)$ is defined as follows:

$$f(\varepsilon)=\begin{cases} E\varepsilon \text{ for } \varepsilon<\varepsilon_y \\ f_y \text{ for } \varepsilon_y<\varepsilon\le\varepsilon_{sh} \\ f_y+(f_u-f_y)\left\{K_1\left(\frac{\varepsilon-\varepsilon_{sh}}{\varepsilon_u-\varepsilon_{sh}}\right)+\frac{K_2\left(\frac{\varepsilon-\varepsilon_{sh}}{\varepsilon_u-\varepsilon_{sh}}\right)}{\left[1+K_3\left(\frac{\varepsilon-\varepsilon_{sh}}{\varepsilon_u-\varepsilon_{sh}}\right)^{K_4}\right]^{\frac{1}{K_4}}}\right\} \text{ for } \varepsilon_{sh}<\varepsilon\le\varepsilon_u \end{cases} \quad \text{Eq. 2}$$

where ε_y denotes the strain at the onset of yielding, ε_{sh} the strain at the start of the strain-hardening phase. The model parameters K_1, K_2, K_3 and K_4 were previously calibrated by Yun and Gardner [47] for hot-rolled steels, with values of 0.4, 2, 400 and 5, respectively. Fig. 15 presents the comparison between the experimental stress–strain curves and those predicted by the model. For each heat input condition, one representative curve is shown, as the mechanical response exhibited minimal scatter and isotropic behaviour across different orientations. The figure also includes the average relative error between the experimental and predicted values for each condition. The results indicate that the model closely reproduces the experimental behaviour, with average relative errors ranging from 1.85 % to 3.00 %. This suggests that the parameters calibrated for hot-rolled steels may be applicable to WAAM components produced under the tested processing conditions.

4. Predictive modelling of WAAM process-structure-property relationships

4.1. Proposed expressions

This section integrates the empirical models established throughout the study. The main goal is to facilitate predictive planning and

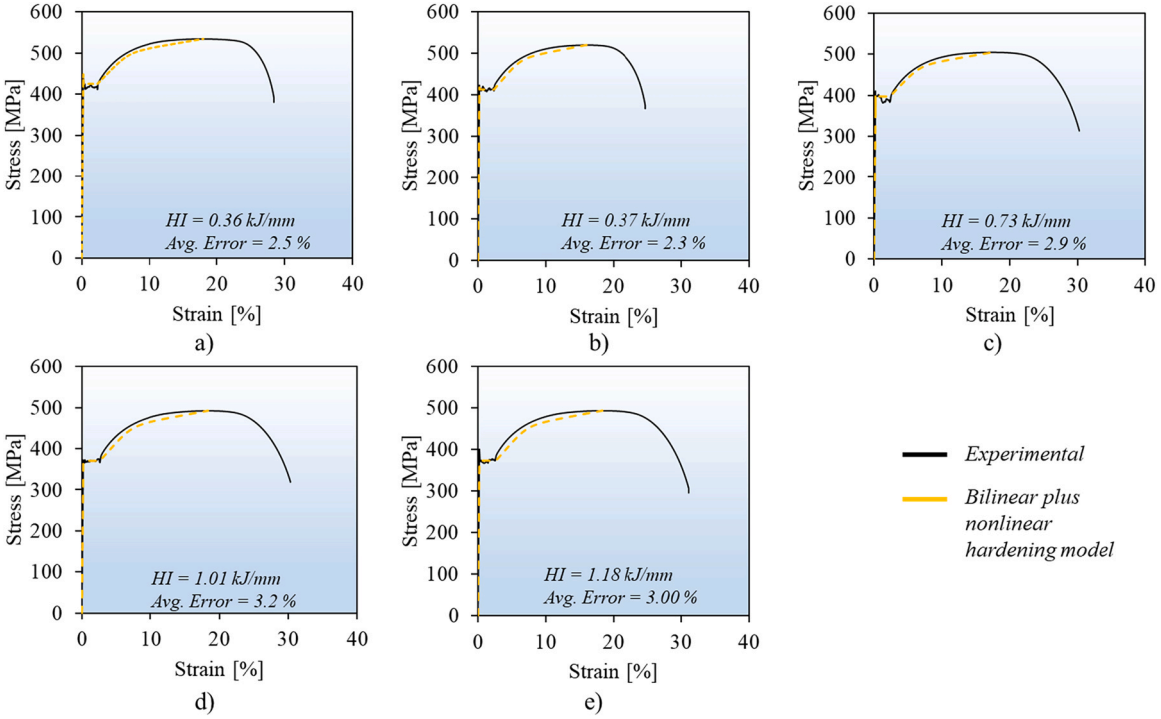

Fig. 15. Comparison between experimental stress–strain curves and predictions from the bilinear plus nonlinear hardening model [47].

optimisation of WAAM processes by linking key process parameters to the resulting thermal, geometric, and mechanical characteristics of the fabricated walls. It was observed that the primary process outcomes can be effectively described using two coefficients, the deposition index given by the *WFS/TS*, which governs the volumetric feed rate per unit length and the HI, calculated according to Eq. 1, which controls the thermal energy delivered per unit length. Together, these coefficients enable the modelling of the process–structure–property relationships. Table 10 summarises the fitted relationships and highlights how these two coefficients influence the main WAAM outputs. For the cooling time, bead width, and layer height, the constants were derived based on measurements from the tenth deposited layer. In Table 10, w and h denote the bead width and layer height, respectively.

These equations may serve to construct process maps that visually delineate optimal operating conditions for different design objectives. Such tools enable tailored parameter selection and support property-driven slicing strategies in WAAM, contributing to the transition from empirical parameter tuning to predictive, model-based fabrication. For the synergic curve used for the P-GMAW, shown in Fig. 2, the processing maps are shown as an example in Fig. 16. Each contour map captures the predicted evolution of the $\Delta t_{8/5}$ cooling time, bead geometry (height and width), and mechanical properties (hardness, yield strength, ultimate tensile strength and ultimate strain) as a function of current and travel speed. These maps can be used to identify feasible process windows that align with specific manufacturing goals, such as maximising strength while controlling bead size for dimensional accuracy.

4.2. Validation

To assess the predictive capability of the proposed analytical models across all parameters analysed in this study, a comprehensive validation was performed. The objective of this section is to evaluate the accuracy of the equations presented in Table 8 by comparing the model outputs with the corresponding experimental data.

The results of this validation are represented in Fig. 17, where predicted values are plotted against experimentally measured data for each target variable. These include $\Delta t_{8/5}$, w, h, HV, f_y, f_u and ε_u. For the $\Delta t_{8/5}$, w and h, the results were derived from measurements taken on the tenth deposited layer. Each subplot presents a parity plot with a red dashed line indicating the ideal 1:1 correspondence between predicted and experimental values. Additionally, the coefficient of determination (R^2) and the average absolute error (in %) are reported for each case to quantitatively assess model performance. As shown in Fig. 17, the developed models exhibit strong predictive accuracy across all target variables. For the majority of cases, the R^2 exceeds 0.9, and the average absolute error remains below 10 %. Predictions related to mechanical properties, such as f_y, f_u and ε_u display particularly low deviations. The model for cooling time ($\Delta t_{8/5}$) shows the highest average error (~18 %), likely due to its sensitivity to arc instability, which continuously adjusts voltage and current values during deposition, and from minor variations associated with surface irregularities. Improved control of wire stick-out and better management of heat accumulation, particularly during the initial layers before steady-state thermal conditions are reached, can further reduce these sources of variation.

It should be noted that the constants defined in Table 10 were validated only against the experimental results obtained in this study, as for most works in the literature this manufacturing data is either not available, not presented in a systematic manner, or is only based on a very narrow parameter range, as observed in the studies summarised in Table 1. Slight variations in these constants may be expected if applied to other WAAM setups, particularly when using different experimental conditions such as interlayer temperature or time, active cooling, deposition strategy, welding wire batch, substrate thickness, among others. Despite these considerations, the overall agreement between predicted and experimental results confirms the robustness of the modelling approach. These outcomes demonstrate the potential of the proposed equations to support parameter selection and performance-driven optimisation in WAAM-fabricated AM46 steel components.

Table 10
Summary of fitted relationships linking process coefficients to WAAM outputs.

Output variable	Governing coefficients	Fitted equation	Constants
Cooling time, $\Delta t_{8/5}$ [s]	*HI*	$\Delta t_{8/5} = a_i HI$	$a_i = 32.47$
Bead width, w [mm]	*WFS/TS; HI*	$w = a_w \left(\frac{WFS}{TS} HI\right)^{B_w}$	$a_w = 3.96$; $B_w = 0.34$
Layer height, h [mm]	*WFS/TS; HI*	$h = a_h \left(\sqrt{\frac{WFS}{TS}} HI^{-0.2}\right)^{B_h}$	$a_h = 0.22$; $B_h = 1.32$
Hardness, HV [$HV_{0.5}$]	*HI*	$HV = a_{HV} HI^{-B_{HV}}$	$a_{HV} = 169.90$; $B_{HV} = 0.10$
Yield strength, f_y [MPa]	*HI*	$f_y = a_{f_y} HI^{-B_{f_y}}$	$a_{f_y} = 373.82$; $B_{f_y} = 0.07$
Ultimate tensile strength, f_u [MPa]	*HI*	$f_u = a_{f_u} HI^{-B_{f_u}}$	$a_{f_u} = 489.79$; $B_{f_u} = 0.04$
Ultimate strain, ε_u [%]	*HI*	$\varepsilon_u = a_{\varepsilon_u} HI^{B_{\varepsilon_u}}$	$a_{\varepsilon_u} = 18.66$; $B_{\varepsilon_u} = 0.05$

5. Conclusion

This study systematically investigated the influence of process parameters and metal transfer modes on the thermal, geometrical, microstructural, and mechanical performance of WAAM low-carbon steel walls. Through a comprehensive experimental campaign and predictive modelling, the following conclusions were drawn:

- The WAAM process window was thoroughly mapped by varying current, voltage, and travel speed. Current levels between 60 and 300 A and travel speeds lower than 10 mm/s promoted stable and continuous deposition, forming defect-free walls.
- The cooling time $\Delta t_{8/5}$ increased linearly with heat input, ranging from approximately 1 s for the first layer deposited at the lowest heat input to a maximum of 46 s for the tenth layer at the highest heat input. The metal transfer mode had negligible influence on the cooling times, showing that the thermal cycles are primarily governed by the energy input.
- Microstructural observations confirmed that low heat input (0.11 kJ/mm) produced walls with refined ferrite-pearlite structures with grain sizes around 4.7 ± 2.5 μm, while high heat input (1.05 kJ/mm) resulted in coarser grains averaging 6.3 ± 4.2 μm. Similar microstructures were observed across CMT, S-GMAW, and P-GMAW processes at equivalent heat inputs, confirming that thermal conditions, rather than transfer mode, governed microstructural evolution.
- Bead width, ranging from 2 mm to 16 mm, and layer height, ranging from 0.8 mm to 4 mm, were accurately predicted using power-law models incorporating the WFS/TS ratio and heat input. These findings confirm that volumetric deposition rate and arc energy are the dominant factors controlling wall geometry.
- All tensile samples fulfilled the ductility requirements defined in Eurocode 3. Yield strength values ranged from 362 MPa to 414 MPa, and ultimate tensile strength from 482 MPa to 520 MPa. Ultimate strain was consistently above 15 % across all tested conditions, confirming adequate ductile behavior for structural applications. The Young's modulus showed moderate variation between 179 GPa and 219 GPa. Mechanical anisotropy was minimal, with less than 4 % variation in strength and ductility across build orientations.
- Empirical models based on WFS/TS and heat input successfully predicted key outcomes, including bead geometry, hardness, and mechanical properties. These models were implemented in process maps that visualise the effects of current and travel speed across the

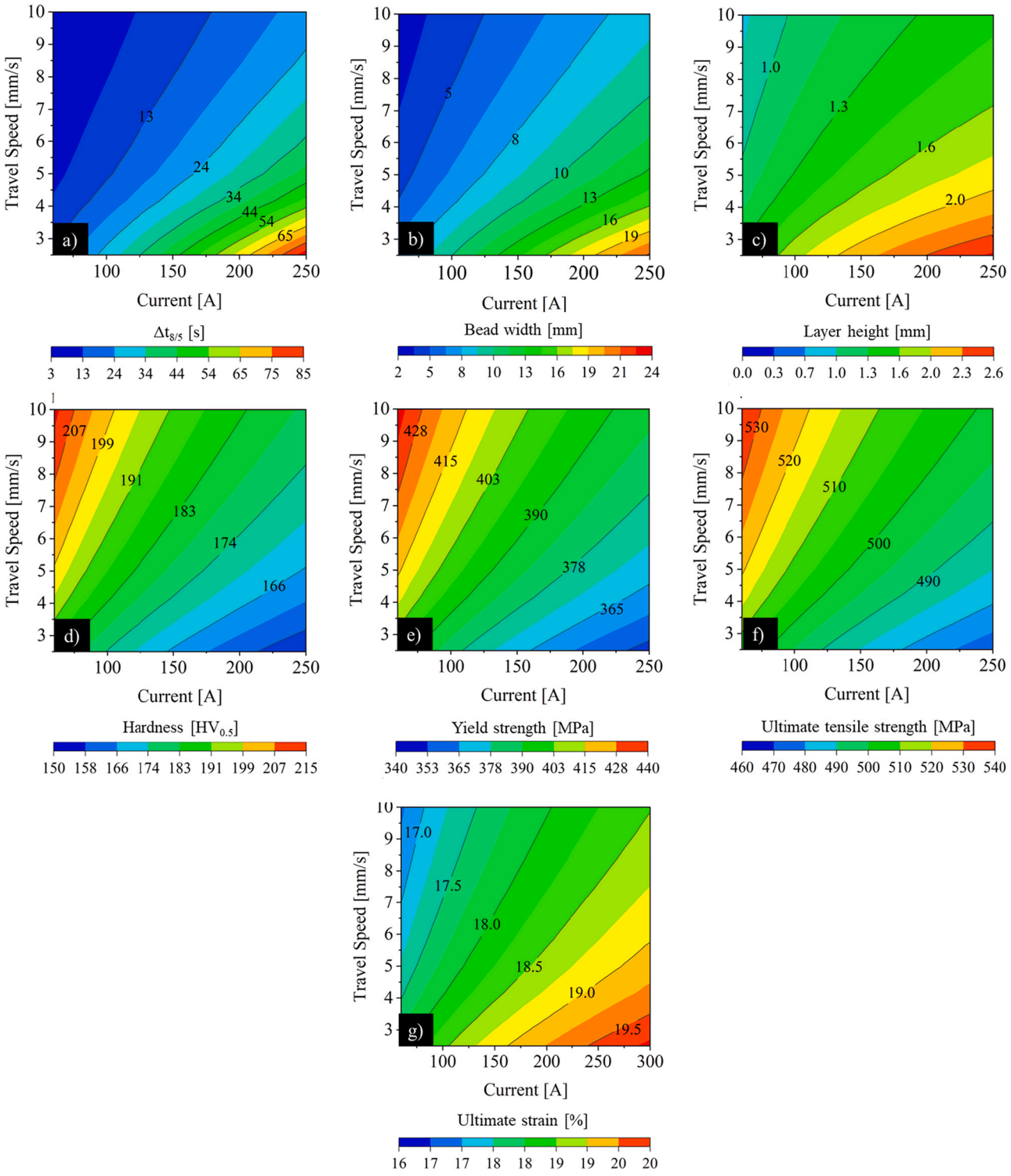

Fig. 16. Process maps derived from the fitted empirical models showing the predicted influence of the welding current and travel speed on the (a) $\Delta t_{8/5}$ cooling time, (b) layer height, (c) layer width, (d) hardness, (e) yield strength, (f) ultimate tensile strength and (g) ultimate strain.

tested range. Such tools support property-driven slicing, optimisation of mechanical performance, and robust parameter planning for industrial WAAM applications.

- The predictive models developed for the process–structure–property relationships demonstrated strong correlation with the experimental data, with R^2 values typically above 0.9 and average errors below 10 %. Although minor scatter was observed, particularly the $\Delta t_{8/5}$ cooling time and ultimate strain ε_u, the overall agreement confirms the reliability of the models in capturing key trends and supporting process optimisation in WAAM of AM46 carbon steel.
- All three metal transfer modes (CMT, S-GMAW, and P-GMAW) exhibited comparable process stability, microstructural features, and mechanical performance within the investigated range. Stable, defect-free deposition was consistently achieved with currents between 100 and 300 A and travel speeds below 10 mm/s, typically 3–8 mm/). To enhance mechanical strength and refine the

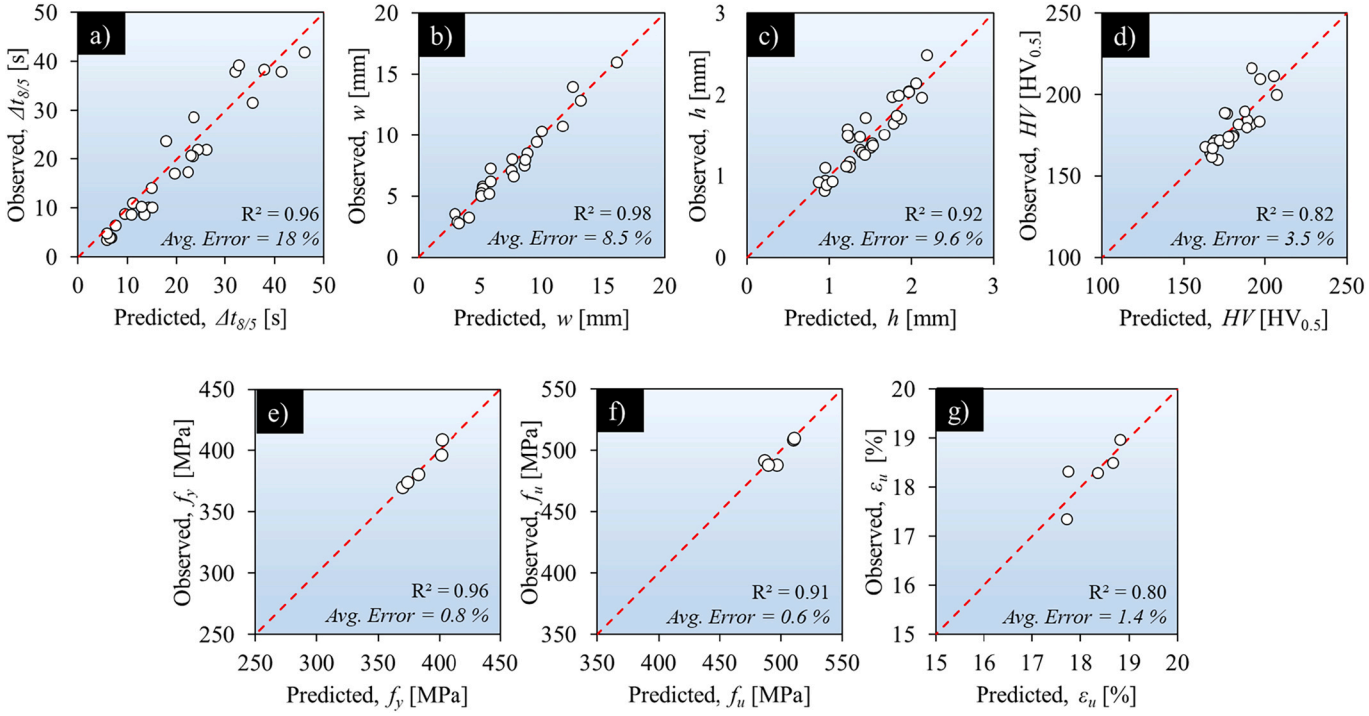

Fig. 17. Comparison between predicted and experimental values for all analytical models developed: (a) cooling time ($\Delta t_{8/5}$), (b) bead width (w), (c) layer height (h), (d) hardness (HV), (e) yield strength (f_y), (f) ultimate tensile strength (f_u), (g) and ultimate strain (ε_u). Dashed red lines represent the ideal 1:1 correlation. R^2 and average absolute error values indicate the model accuracy for each property.

ferrite–pearlite microstructure, lower heat inputs within this window are recommended.

CRediT authorship contribution statement

C. Zhu: Writing – review & editing, Methodology, Investigation, Formal analysis. **T. Tankova:** Writing – review & editing, Writing – original draft, Supervision, Methodology, Funding acquisition, Formal analysis, Conceptualization. **D.G. Andrade:** Writing – review & editing, Writing – original draft, Visualization, Methodology, Investigation, Formal analysis. **L. Simões da Silva:** Writing – review & editing, Writing – original draft, Supervision, Funding acquisition, Conceptualization. **H. El Bamby:** Visualization, Investigation, Formal analysis. **S. Sabari:** Writing – review & editing, Writing – original draft, Resources. **K. Monteiro:** Visualization, Investigation.

Declaration of Competing Interest

I declare on behalf of myself and all the authors that there is no conflict of interest.

Acknowledgements

This work has received funding from: - The Research Fund for Coal and Steel under grant agreement 101112614 — IAMFat.

-This work was partly financed by FCT/MCTES under the R&D Unit Institute for Sustainability and Innovation in Structural Engineering (ISISE), under the references UID/4029/2025 (https://doi.org/10.54499/UID/04029/2025) and UID/PRR/04029/2025 (https://doi.org/10.54499/UID/PRR/04029/2025), and under the Associate Laboratory Advanced Production and Intelligent Systems ARISE under reference LA/P/0112/2020.

-This work was partly funded by national funds through FCT – Foundation for Science and Technology, under grant agreement 2021.05992.BD attributed to C. Zhu.

- This work was partly funded by national funds through FCT – Foundation for Science and Technology, under grant agreement 2022.11969.BD attributed to K. Monteiro.

References

[1] Priarone PC, Campatelli G, Catalano AR, Baffa F. Life-cycle energy and carbon saving potential of wire arc additive manufacturing for the repair of mold inserts. CIRP J Manuf Sci Technol 2021;35:943–58. https://doi.org/10.1016/j.cirpj.2021.10.007.

[2] Baqershahi MH, Ayas C, Ghafoori E. Topology optimisation for large-scale wire-arc directed energy deposition considering environmental impact and cost. Autom Constr 2025;177:106313. https://doi.org/10.1016/j.autcon.2025.106313.

[3] Laghi V, Savino E, Gasparini G. Reduction of the environmental impact of complex-shaped steel joints through topology optimization and large-scale metal 3D printing. Results Eng 2025;27:105610. https://doi.org/10.1016/j.rineng.2025.105610.

[4] Weman K. Power sources for arc welding. Svetsaren 2003;58:30–2.

[5] Mukherjee M, Saha S, Pal TK, Kanjilal P. Influence of modes of metal transfer on grain structure and direction of grain growth in low nickel austenitic stainless steel weld metals. Mater Charact 2015;102:9–18. https://doi.org/10.1016/j.matchar.2015.02.006.

[6] Zhu L, Luo Y, Han J, Zhang C, Xu J, Chen D. Energy characteristics of droplet transfer in wire-arc additive manufacturing based on the analysis of arc signals. Meas J Int Meas Confed 2019;134:804–13. https://doi.org/10.1016/j.measurement.2018.10.048.

[7] Luo Y, Li J, Xu J, Zhu L, Han J, Zhang C. Influence of pulsed arc on the metal droplet deposited by projected transfer mode in wire-arc additive manufacturing. J Mater Process Technol 2018;259:353–60. https://doi.org/10.1016/j.jmatprotec.2018.04.047.

[8] Wang Y, Chen J, Chen M, Su H, Zong R, Wu D, Komen H, Tanaka M, Wu C. A comparative study on microstructure and mechanical properties of wire-arc directed energy deposited Al–Zn–Mg–Cu alloy based on the cold metal transfer technology. J Mater Res Technol 2024;30:397–415. https://doi.org/10.1016/j.jmrt.2024.03.073.

[9] Selvi S, Vishvaksenan A, Rajasekar E. Cold metal transfer (CMT) technology - An overview. Def Technol 2018;14:28–44. https://doi.org/10.1016/j.dt.2017.08.002.

[10] He S, Yang D, Huang Y, Wang K. Effect of the current waveform on the droplet transfer in CMT welding high-nitrogen steel. J Manuf Process 2022;75:41–8. https://doi.org/10.1016/j.jmapro.2022.01.013.

[11] Dinovitzer M, Chen X, Laliberte J, Huang X, Frei H. Effect of wire and arc additive manufacturing (WAAM) process parameters on bead geometry and microstructure. Addit Manuf 2019;26:138–46. https://doi.org/10.1016/j.addma.2018.12.013.

[12] Šćetinec A, Klobčar D, Bračun D. In-process path replanning and online layer height control through deposition arc current for gas metal arc based additive manufacturing. J Manuf Process 2021;64:1169–79. https://doi.org/10.1016/j.jmapro.2021.02.038.
[13] da Silva LJ, Scotti FM, Fernandes DB, Reis RP, Scotti A. Effect of O2 content in argon-based shielding gas on arc wandering in WAAM of aluminum thin walls. CIRP J Manuf Sci Technol 2021;32:338–45. https://doi.org/10.1016/j.cirpj.2021.01.018.
[14] Yamaguchi M, Komata R, Furumoto T, Abe S, Hosokawa A. Influence of metal transfer behavior under Ar and CO2 shielding gases on geometry and surface roughness of single and multilayer structures in GMAW-based wire arc additive manufacturing of mild steel. Int J Adv Manuf Technol 2022;119:911–26. https://doi.org/10.1007/s00170-021-08231-8.
[15] Marefat F, Kapil A, Banaee SA, Van Rymenant P, Sharma A. Evaluating shielding gas-filler wire interaction in bi-metallic wire arc additive manufacturing (WAAM) of creep resistant steel-stainless steel for improved process stability and build quality. J Manuf Process 2023;88:110–24. https://doi.org/10.1016/j.jmapro.2023.01.046.
[16] Ding C, Cui X, Jiao J, Zhu P. Effects of substrate preheating temperatures on the microstructure, properties, and residual stress of 12CrNi2 prepared by laser cladding deposition technique. Materials 2018;11. https://doi.org/10.3390/ma11122401.
[17] Gurmesa F, Lemu H, Adugna Y, Harsibo M. Residual stresses in wire arc additive manufacturing products and their measurement techniques: a systematic review. Appl Mech 2024;5:420–49. https://doi.org/10.3390/applmech5030025.
[18] Gudur S, Nagallapati V, Pawar S, Muvvala G, Simhambhatla S. A study on the effect of substrate heating and cooling on bead geometry in wire arc additive manufacturing and its correlation with cooling rate. Mater Today Proc 2019;41:431–6. https://doi.org/10.1016/j.matpr.2020.10.071.
[19] Adebayo A, Mehnen J, Tonnellier X. Limiting travel speed in additive layer manufacturing. ASM Proc Int Conf Trends Weld Res 2013;3:1038–44.
[20] Rosli NA, Alkahari MR, Abdollah MF bin, Maidin S, Ramli FR, Herawan SG. Review on effect of heat input for wire arc additive manufacturing process. J Mater Res Technol 2021;11:2127–45. https://doi.org/10.1016/j.jmrt.2021.02.002.
[21] Mohammadi J, Dashtgerd I, Reza Riahi A, Mostafaei A. Pulsed gas metal arc additive manufacturing of low-carbon steel: microstructure observations and mechanical properties. Mater Today Commun 2024;38:107637. https://doi.org/10.1016/j.mtcomm.2023.107637.
[22] Panicker C.T J, Senthilkumar V. Effect of arc rotation on the enhancement of mechanical properties of ER70S6 in WAAM. Vacuum 2024;220:112837. https://doi.org/10.1016/j.vacuum.2023.112837.
[23] Dekis M, Tawfik M, Egiza M, Dewidar M. Unveiling the characteristics of ER70S-6 low carbon steel alloy produced by wire arc additive manufacturing at different travel speeds. Met Mater Int 2024:325–38. https://doi.org/10.1007/s12540-024-01766-x.
[24] Zhai W, Guo Y, Aishwarya, Canturri C, Shandro R, Zhou W. Wire arc additive manufacturing of ER70S-6/S355 bimetal component. Mater Sci Eng A 2024;900:146498. https://doi.org/10.1016/j.msea.2024.146498.
[25] Badoniya P, Srivastava M, Jain PK. Parametric influence and effect of cooling channel on bead geometry profiles of ER70S-6 manufactured using wire arc additive manufacturing. Mater Today Proc 2024. https://doi.org/10.1016/j.matpr.2024.04.076.
[26] Huang C, Kyvelou P, Zhang R, Ben Britton T, Gardner L. Mechanical testing and microstructural analysis of wire arc additively manufactured steels. Mater Des 2022;216:110544. https://doi.org/10.1016/j.matdes.2022.110544.
[27] Bellamkonda PN, Sudersanan M, Visvalingam B. A study on tensile properties and microstructural characteristics of wire arc additive manufactured low carbon steel cylindrical components. Weld Int 2022;36:443–54. https://doi.org/10.1080/09507116.2022.2097897.
[28] Xin H, Tarus I, Cheng L, Veljkovic M, Persem N, Lorich L. Experiments and numerical simulation of wire and arc additive manufactured steel materials. Structures 2021;34:1393–402. https://doi.org/10.1016/j.istruc.2021.08.055.
[29] Aldalur E, Veiga F, Suárez A, Bilbao J, Lamikiz A. High deposition wire arc additive manufacturing of mild steel: strategies and heat input effect on microstructure and mechanical properties. J Manuf Process 2020;58:615–26. https://doi.org/10.1016/j.jmapro.2020.08.060.
[30] Dirisu P, Ganguly S, Mehmanparast A, Martina F, Williams S. Analysis of fracture toughness properties of wire + arc additive manufactured high strength low alloy structural steel components. Mater Sci Eng A 2019;765:138285. https://doi.org/10.1016/j.msea.2019.138285.
[31] Chen X, Sun Y. Experimental investigation of mechanical properties of 3D-printed normal-strength and high-strength steels. J Constr Steel Res 2025;234:109773.
[32] Rafieazad M, Ghaffari M, Vahedi Nemani A, Nasiri A. Microstructural evolution and mechanical properties of a low-carbon low-alloy steel produced by wire arc additive manufacturing. Int J Adv Manuf Technol 2019;105:2121–34. https://doi.org/10.1007/s00170-019-04393-8.
[33] Le VT, Mai DS, Hoang QH. A study on wire and arc additive manufacturing of low-carbon steel components: process stability, microstructural and mechanical properties. J Braz Soc Mech Sci Eng 2020;42:1–11. https://doi.org/10.1007/s40430-020-02567-0.
[34] Ayan Y, Kahraman N. Wire arc additive manufacturing of low-carbon mild steel using two different 3D printers. Phys Met Metallogr 2021. https://doi.org/10.1134/S0031918X21140039.
[35] Astarita A, Campatelli G, Corigliano P, Epasto G, Montevecchi F, Scherillo F, Venturini G. Microstructure and mechanical properties of specimens produced using the wire-arc additive manufacturing process. Proc Inst Mech Eng Part C J Mech Eng Sci 2021;235:1788–98. https://doi.org/10.1177/0954406219883324.
[36] Tankova T, Andrade D, Branco R, Zhu C, Rodrigues D, Simões da Silva L. Characterization of robotized CMT-WAAM carbon steel. J Constr Steel Res 2022;199. https://doi.org/10.1016/j.jcsr.2022.107624.
[37] Nagasai BP, Malarvizhi S, Balasubramanian V. Effect of welding processes on mechanical and metallurgical characteristics of carbon steel cylindrical components made by wire arc additive manufacturing (WAAM) technique. CIRP J Manuf Sci Technol 2022;36:100–16. https://doi.org/10.1016/j.cirpj.2021.11.005.
[38] Monteiro K, Zhu C, Santos AF, da Silva LS, Tankova T. Integrated topological optimization and production of an additively manufactured steel T-joint: a case study. Structures 2025;74. https://doi.org/10.1016/j.istruc.2025.108511.
[39] Welding BSI. BS EN 1011-1:2009. Welding — recommendations for welding of metallic materials. Part 1 Gen Guid Arc Weld 2001.
[40] Andrade DG, Zhu C, Miranda HC, Rodrigues DM. Thermal, Microstructural, and mechanical analysis of complex lattice structures produced by direct energy deposition. Materials 2024. https://doi.org/https://doi.org/10.3390/ma17122813.
[41] ASTM, ASTM E3-11(2017) - Standard Guide for Preparation of Metallographic Specimens, (2017).
[42] ISO-6892-1, Metallic materials – Tensile Testing – Part 1: Method of Test at Room Temperature, (2019).
[43] Yang D, Wang G, Zhang G. Thermal analysis for single-pass multi-layer GMAW based additive manufacturing using infrared thermography. J Mater Process Technol 2017;244:215–24. https://doi.org/10.1016/j.jmatprotec.2017.01.024.
[44] Long J, Wang M, Zhao W, Zhang X, Wei Y, Ou W. High-power wire arc additive manufacturing of stainless steel with active heat management. Sci Technol Weld Join 2022;27:256–64. https://doi.org/10.1080/13621718.2022.2045127.
[45] Andrade DG, Tankova T, Zhu C, Branco R, Simões da L, Rodrigues DM. Mechanical properties of 3D printed CMT-WAAM 316 LSi stainless steel walls. J Constr Steel Res 2024;215. https://doi.org/10.1016/j.jcsr.2024.108527.
[46] CEN, EN 1993-1-1: Eurocode 3: Design of Steel Structures – Part 1-1: General Rules and Rules for Buildings. Brussels: European Committee for Standardization, (2014).
[47] Yun X, Gardner L. Stress-strain curves for hot-rolled steels. J Constr Steel Res 2017;133:36–46. https://doi.org/10.1016/j.jcsr.2017.01.024.